Variational assimilation of satellite observations in a coastal ocean model off Oregon

A. L. Kurapov,[1] D. Foley,[2] P. T. Strub,[1] G. D. Egbert,[1] and J. S. Allen[1]

[1] Satellite along-track sea surface height (SSH) and multisatellite sea surface temperature (SST) maps are assimilated in a coastal ocean circulation model off Oregon. The study period is June–October 2005, featuring intensive separation of the coastal upwelling jets in the eddy-dominated coastal transition zone (CTZ). The data assimilation (DA) system combines the nonlinear Regional Ocean Modeling System (ROMS) and the Advanced Variational Regional Ocean Representer Analyzer (AVRORA) tangent linear and adjoint codes developed by our group. The variational representer DA method is implemented in a series of 6 day time windows, with initial conditions corrected at the beginning of each window. To avoid the problem of matching the model and observed SSH mean levels, the observed SSH slope has been assimilated. Location, timing, and intensity of jets and eddies in the CTZ are constrained, to improve accuracy of nonlinear model analyses and forecasts. In the case assimilating SSH alone, the geometry of the SST front is improved. SSH assimilation results in the cross-shore transport more uniformly distributed along the coast than in the free run model. An outer front is identified in the DA analyses at a distance of 200 km from the coast. A strong subsurface horizontal temperature gradient across this front influences the depth of the thermocline in an area between the front and the continental slope. The DA correction term is comparable in magnitude to dominant terms in the volume-integrated heat equation. The time-averaged DA correction term in the volume-integrated heat balance is closer to 0 in the combined SSH-SST assimilation case, than in the case assimilating SSH alone.

Citation: Kurapov, A. L., D. Foley, P. T. Strub, G. D. Egbert, and J. S. Allen (2011), Variational assimilation of satellite observations in a coastal ocean model off Oregon, *J. Geophys. Res.*, *116*, C05006, doi:10.1029/2010JC006909.

1. Introduction

[2] Accurate forecasts of transports and hydrographic conditions in the coastal ocean can be important in many applications including naval operations, shipping, search and rescue, and environmental hazard response. Data assimilation (DA) methods have been developed to optimally combine observations and ocean models, to provide the best estimate of ocean conditions and initial conditions for forecasts. The topic of this paper is on whether assimilation of satellite observations of sea surface height (SSH) and sea surface temperature (SST) is useful for prediction in the coastal ocean. The study is focused on the area off the Oregon coast (northwestern United States, Figure 1) where shelf circulation in summer is forced by the predominantly southward wind stress (Figure 2) resulting in coastal upwelling and energetic southward alongshore currents.

As summer upwelling progresses, shelf currents separate offshore in the coastal transition zone (CTZ) [*Brink and Cowles*, 1991; *Koch et al.*, 2010], where dynamics are dominated by nonlinear transformations of energetic jets and eddies. Upwelling at the coast and separation of cold filaments in the CTZ can be readily observed in satellite SST imagery. The slope of SSH estimated from satellite altimetry is related to surface geostrophic currents that can be associated with jets and eddies in the CTZ.

[3] Our study period is June–October 2005 when information from three satellite altimeters with distinct orbits is available, including TOPEX, Jason, and Envisat (Figure 3). In that year, a combination of warmer than average near-surface temperatures and no sustained southward wind stress in spring (Figure 2) resulted in a 2 month delay in the start of sustained upwelling on the mid-Oregon shelf, which is usually characterized by a distinctive cold water signature near surface [*Kosro et al.*, 2006; *Schwing et al.*, 2006; *Pierce et al.*, 2006]. Despite the late start, separation of cold upwelled waters in the CTZ by the end of summer (e.g., August and September) was more vigorous than in most other years.

[4] The distance between parallel TOPEX or Jason tracks is approximately 250 km, with measurements repeated along

[1]College of Oceanic and Atmospheric Sciences, Oregon State University, Corvallis, Oregon, USA.
[2]Environmental Research Division, NOAA Southwest Fisheries Science Center, Pacific Grove, California, USA.
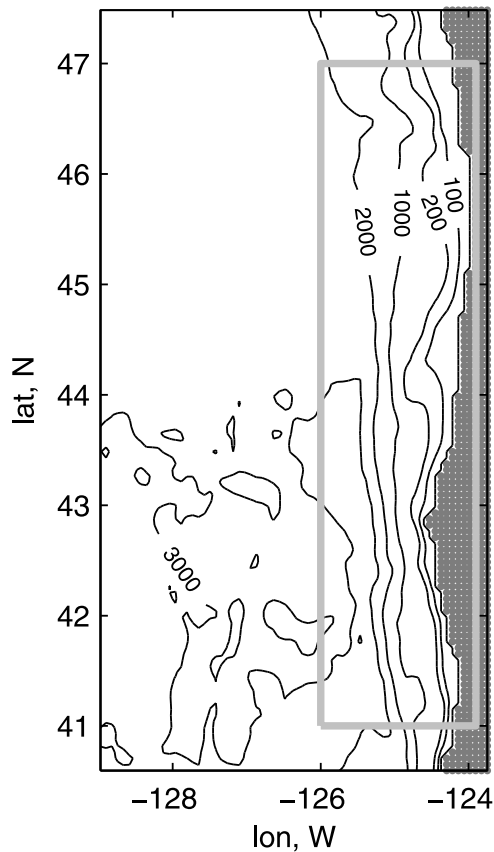
Figure 1. Model domain. Bathymetric contours are at 100, 200, 1000, 2000, and 3000 m. The gray box shows the area of integration for the heat equation term balance analyses (section 5.4).

each track once every 10 days. The Envisat tracks are closer, about 60 km apart, and repeated once every 35 days. To create SSH maps from these along-track measurements, traditional data analysis methods would use interpolation (covariance) functions with large space and time decorrelation scales. As a result, the small-scale and anisotropic SSH signal associated with narrow (a few tens of km wide), but intensive (sometimes >0.5 m s^{-1}) near-surface CTZ jets

would be misrepresented (smeared) in the SSH maps. To utilize the useful signal in the altimetry on spatial scales <100 km, we assimilate along-track SSH data in a high-resolution ocean circulation model. The variational DA method utilized can be viewed as objective mapping, in which an anisotropic, multivariate covariance is provided by the dynamical model [*Bennett*, 2002].

[5] Variational DA finds corrections to model inputs by minimizing the cost function, which is a sum of quadratic penalties on the errors (corrections) in these inputs (e.g., in our case, initial conditions) and observation-model differences, all integrated over the model domain and a specified time interval. Minimization algorithms require repeated runs of a tangent linear (TL) version of the model and its adjoint counterpart (ADJ). In this study we use our own TL and ADJ codes (Advanced Variational Regional Ocean Representer Analyzer (AVRORA)), combined with the nonlinear model based on Regional Ocean Modeling System (ROMS, www.myroms.org). Our TL code is dynamically and algorithmically consistent with ROMS. The AVRORA-ROMS DA system is built following principles developed for the modular Inverse Ocean Modeling System [*Bennett et al.*, 2008]. Although TL and ADJ ROMS components have been available [*Di Lorenzo et al.*, 2007; *Broquet et al.*, 2009; *Powell et al.*, 2009], AVRORA has offered us more flexibility in the choice of model input error covariances (section 3) and data functionals (matching observations and model outputs, section 4) than the current version of community TL and ADJ ROMS provides. *Kurapov et al.* [2009] tested the AVRORA-ROMS DA system with idealized (model generated) observations in a coastal upwelling system. The present manuscript describes the first implementation of this system with actual observations of SSH and SST. We will demonstrate (section 5) the positive effect of the along-track altimetry assimilation on the geometry of the modeled SST front, describe some newly discovered features in the CTZ, and analyze the relative contribution of the DA to the model heat balance.

2. The Model

[6] The model domain (Figure 1) includes the entire Oregon and parts of the Washington and California coasts. The offshore extent is approximately 350 km. ROMS,
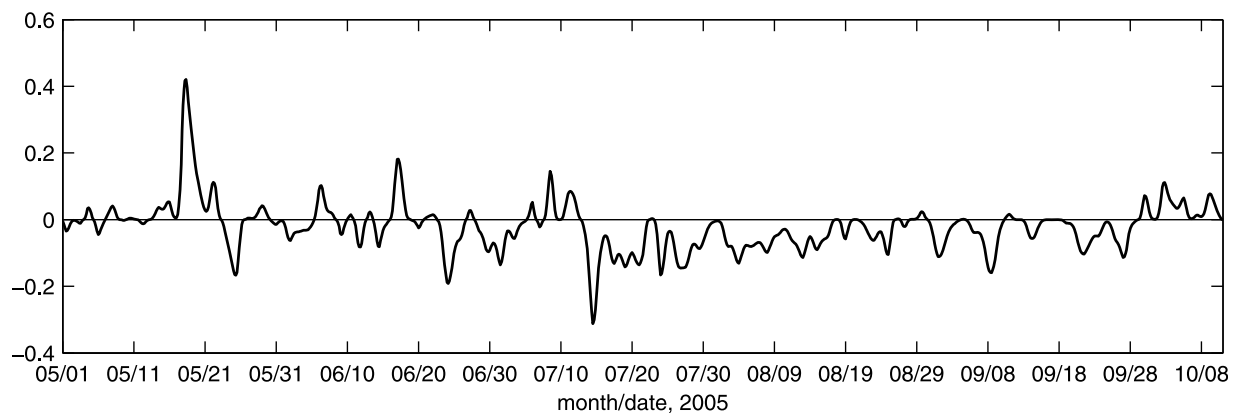

Figure 2. Model meridional wind stress (N m^{-2}) over a shelf edge location at 45°N, 200 m depth.
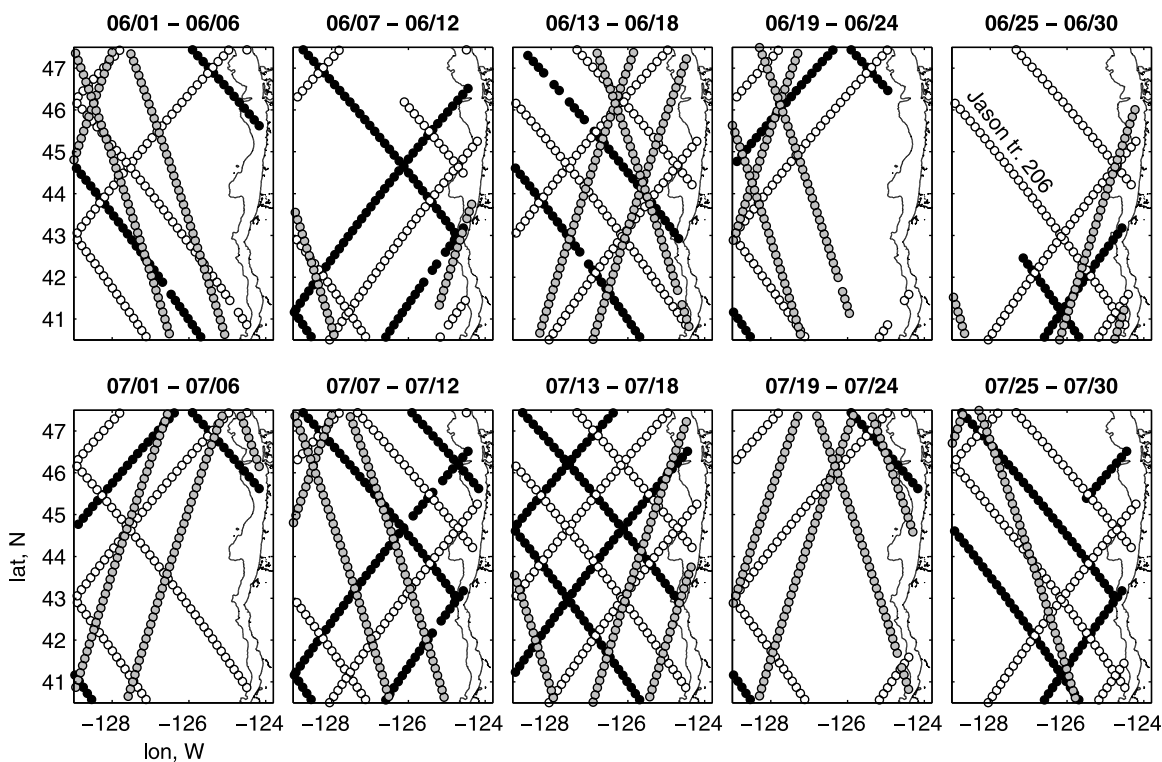
Figure 3. Locations of AVISO along-track satellite altimeter data available in a series of several 6 day assimilation windows, 1 June to 30 July 2005, TOPEX (black), Jason (white), and Envisat (gray). The bathymetric contour shown is 200 m.

utilized as the nonlinear component in our DA system, is a primitive equation, hydrostatic, Boussinesq model using terrain-following coordinates in the vertical. Subgrid turbulence is parameterized using the level 2.5 Mellor-Yamada scheme [*Mellor and Yamada*, 1982; *Wijesekera et al.*, 2003]. Process-oriented studies and extensive model-data comparisons of summer circulation have been performed in a similar domain using ROMS at the 3 km horizontal resolution [*Springer et al.*, 2009; *Kim et al.*, 2009; *Koch et al.*, 2010]. Since variational DA requires repeated runs of the TL and ADJ codes, its computational cost can be on the order of 10–100 times as large as that of the forward nonlinear model run. To approach first tests of the AVRORA assimilation system in a practical manner, we choose a coarser resolution model than that in the above mentioned process-oriented studies, namely, approximately 6 km in horizontal and 15 terrain-following layers in vertical. To compute surface momentum and heat fluxes in the ocean model using the bulk flux formulation in ROMS [*Fairall et al.*, 1996], atmospheric fields (including near-surface wind speed, air temperature, atmospheric pressure, and relative humidity) are obtained from the 12 km resolution Northern America Mesoscale Model (NAM) forecast archives (http://nomads. ncdc.noaa.gov/data.php). These time series fields, provided with 3 h temporal resolution, are smoothed using a 40 h half-amplitude low-pass filter. Oceanic boundary conditions are obtained from daily averaged outputs of the 9 km resolution Navy Coastal Ocean Model of California Current System (NCOM-CCS) [*Shulman et al.*, 2004]. Tides and the Columbia River fresh water flux are not included.

[7] The no DA, free run model solution is obtained for the period of 1 May to 10 October 2005, with initial conditions derived from NCOM-CCS. Despite the limited resolution of the model, it reproduces coastal upwelling and separation of the shelf current near Cape Blanco (42.7°N) qualitatively correctly. For instance, model SSH sampled along Jason track 206 (Figure 4, gray lines) shows variability similar to the data and the slope associated with near-coastal upwelling early in the season is reproduced. Features associated with jets and eddies in the CTZ are also present in the model SSH, with horizontal scales and amplitudes similar to the observed signal, although the location and timing of these features differ between the model and the data. Comparisons with the data along other tracks (not shown) exhibit similar patterns, with generally better model prediction of the SSH slope next to the coast than in the CTZ. Since the model can reproduce scales of SSH variability over the shelf and in the CTZ qualitatively correctly, we anticipate that this model will be receptive to corrections due to assimilation of the along-track SSH data, leading to improved forecasts. Since mesoscale fields of the SSH, currents, and density are dynamically coupled by geostrophy and thermal wind relations, SSH assimilation could potentially improve the geometry of the predicted SST fronts, even if satellite SST maps are not assimilated. Our DA problem is formulated to explore these ideas.

3. The Assimilation Approach

[8] The variational DA method is implemented in a series of 6 day assimilation windows. In each window, e.g.,
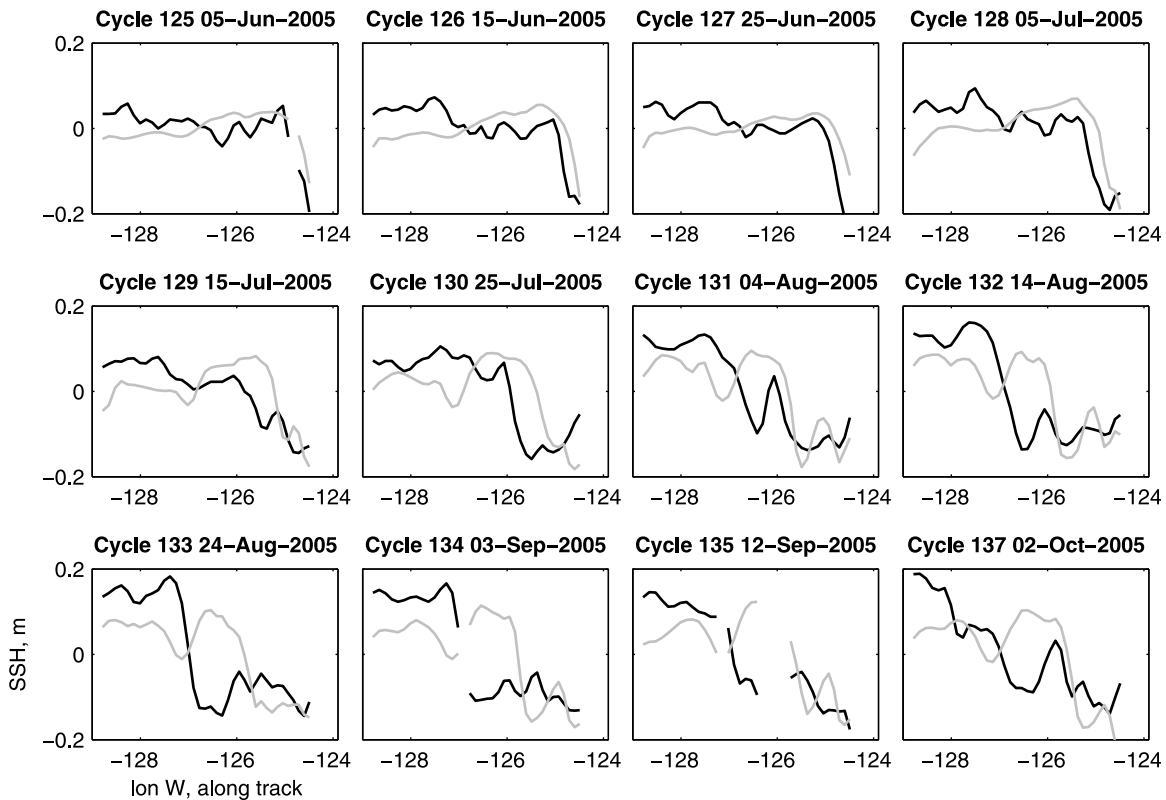
Figure 4. Observed AVISO absolute dynamic topography (black) and model SSH (gray) along Jason track 206, June–October 2005 (see Figure 3 for the track location); each line is demeaned independently.

$t = (0, 6)$ days, observations of along-track SSH, or SSH and SST in combination, are assimilated to correct initial conditions at $t = 0$ days. The nonlinear ROMS solution provides the background state for the TL and ADJ AVRORA codes, which are used to find the correction. Then, the nonlinear ROMS model is run for a period of 12 days ($t = (0, 12)$ days), starting from the corrected initial conditions. The period of $(0, 6)$ days, where data were assimilated, is called the analysis, and $(6, 12)$ days the forecast. In the next assimilation window, $(6, 12)$ days, the forecast solution from the previous window is utilized as the background state for AVRORA linearization and the same assimilation procedure is repeated. The indirect representer minimization algorithm [*Egbert et al.*, 1994; *Chua and Bennett*, 2001; *Bennett*, 2002] is utilized in each assimilation window to find the optimal correction; this combined variational-sequential DA approach is similar to representer cycling [*Xu and Daley*, 2000; *Ngodock et al.*, 2007]. In terms of representer methodology, only one "outer loop" iteration is performed in each window. This means that after the optimal solution is found, it is not used again as the new, improved background to repeat assimilation in the same window. This approach will be justified provided assimilation in a series of windows gradually improves forecasts to make background solutions close enough to the (unknown) true state, such that a single linearized correction is sufficient.

[9] To further explain DA details, it is convenient to represent the model output (trajectory) as a discrete in space and continuous in time vector $\mathbf{u}(t)$. It includes all elements of the two-dimensional (2-D) SSH field ζ and 3-D fields

of horizontal velocity (u, v), temperature T, and salinity S. The nonlinear model is written symbolically as

$$\frac{\partial \mathbf{u}}{\partial t} = M(\mathbf{u}), \tag{1}$$

where M is the nonlinear model operator. In each assimilation window, the background solution $\mathbf{u}^b(t)$ is obtained by integrating (1) with background initial conditions $\mathbf{u}_0^b$. The TL counterpart of $M(\mathbf{u})$ is $\mathbf{A}[\mathbf{u}^b]\mathbf{u}$, where $\mathbf{A}[\mathbf{u}^b]$ is the matrix of elements that depend on the time-variable background trajectory $\mathbf{u}^b$.

[10] The cost function minimized in every 6 day assimilation window, subject to the strong model constraint (1), is

$$J(\mathbf{u}) = \left[\mathbf{u}(0) - \mathbf{u}_0^b\right]'\mathbf{C}_0^{-1}\left[\mathbf{u}(0) - \mathbf{u}_0^b\right] + \left[\mathbf{d} - L\mathbf{u}(t)\right]'\mathbf{C}_d^{-1}\left[\mathbf{d} - L\mathbf{u}(t)\right], \tag{2}$$

where $\mathbf{u}(0)$ is the estimated initial conditions, $\mathbf{d}$ is the data vector (all observations collected in the assimilation time window), L is the operator matching the data vector to the time-dependent model state, $\mathbf{C}_0$ and $\mathbf{C}_d$ are the initial condition and data error covariance matrices, respectively, and the prime sign denotes matrix transpose. One can note that in the case in which only initial conditions are corrected the cost function could alternatively be formulated as a function of initial conditions alone [$J(\mathbf{u}_0)$]. Both formulations would be equivalent. We use formulation (2), which is customary for the representer method [see *Bennett*, 2002], and is readily generalized to cases in which forcing, boundary conditions, and errors in model equations are additionally corrected.

[11] The data functional is the kth element of $L\mathbf{u}$ that matches the model to the kth element of vector $\mathbf{d}$. It can be written as the integral over the assimilation interval $(0, T_a)$

$$(L\mathbf{u})_k \equiv L_k\mathbf{u} = \int_0^{T_a} \mathbf{q}_k'(\tau)\mathbf{u}(\tau)d\tau. \qquad (3)$$

In the simplest case of an observation local in time and space, $\mathbf{q}_k(t)$ is the impulse function at that location and time. More generally, $\mathbf{q}_k(t)$ represents a linear combination of elements of the (spatially discrete) model trajectory. Specific to our study, $\mathbf{q}_k(t)$ can represent the rule for sampling the model SSH slope in the direction of the satellite track, i.e., the along-track difference between adjacent SSH samples. Equation (3) can also imply temporal averaging or filtering of the model field. Note that the TL and ADJ AVRORA components are built in such a way that we can assimilate not only data matching directly elements of the ROMS output state (i.e., ζ, u, v, T, and S at their respective grid locations and output times), but also any linear combination of the elements of that state. The forcing of the ADJ code and sampling of the TL code have been written for this general data functional, and checked for adjoint symmetry, such that introduction of new data types is trivial to the user.

[12] Following the indirect representer method, an optimal set of representer coefficients $\mathbf{b} = \{b_k\}$ of size K (where K is the total number of observations) is determined iteratively using repeatedly both the TL and ADJ models (Appendix A). Then, in the "final sweep", the ADJ model is run backward in time, using initial conditions $\boldsymbol{\lambda}(T_a) = 0$ and forcing by the optimal linear combination of $\mathbf{q}_k(t)$

$$-\partial\boldsymbol{\lambda}/\partial t = \left(\mathbf{A}[\mathbf{u}^b]\right)'\boldsymbol{\lambda} + \sum_{k=1}^{K} b_k\mathbf{q}_k(t). \qquad (4)$$

Optimal initial conditions $\mathbf{u}(0)$ are determined as

$$\mathbf{u}(0) = \mathbf{u}_0^b + \mathbf{C}_0\boldsymbol{\lambda}(0). \qquad (5)$$

[13] The rule by which the matrix-vector product $\mathbf{C}_0\boldsymbol{\lambda}(0)$ is computed must be specified. In the CTZ, a large component of the initial condition error would be associated with the position of nearly geostrophic jets and eddies. Corresponding dynamical relations would imply that errors in SSH, velocity, and density fields are correlated. To introduce these dynamical constraints in the covariance, it is convenient to use the balance operator $\mathbf{B}$ [Weaver et al., 2005], which provides a linear mapping from a subspace representing mutually uncorrelated dynamical fields to the full model state space. In our case, errors in model ζ, u, v, and S can be linearly coupled to errors in T and the depth-integrated volume transport stream function Ψ using the simplified forms of the T-S relation and equation of state, plus the geostrophic relation (Appendix B)

$$\delta\mathbf{u} \equiv \begin{pmatrix} \delta\zeta \\ \delta u \\ \delta v \\ \delta T \\ \delta S \end{pmatrix} = \mathbf{B}\begin{pmatrix} \delta T \\ \delta\Psi \end{pmatrix}. \qquad (6)$$

[14] To facilitate computation of $\mathbf{C}_0\boldsymbol{\lambda}(0)$, we assume that errors in T and Ψ are statistically independent. Then,

$$\mathbf{C}_0\boldsymbol{\lambda}(0) = \langle\delta\mathbf{u}\delta\mathbf{u}'\rangle\boldsymbol{\lambda}(0) = \mathbf{B}\begin{pmatrix} \mathbf{C}_T & 0 \\ 0 & \mathbf{C}_\Psi \end{pmatrix}\mathbf{B}'\boldsymbol{\lambda}(0), \qquad (7)$$

where $\langle\ldots\rangle$ denote statistical ensemble average (expected value), $\mathbf{C}_T = \langle\delta T\delta T'\rangle$, and $\mathbf{C}_\Psi = \langle\delta\Psi\delta\Psi'\rangle$. In the tests discussed in this manuscript, we make no correction to the initial Ψ, in part since our understanding of barotropic flows in the CTZ is limited. Thus we take $\mathbf{C}_\Psi = 0$. The covariance of initial errors in temperature $\mathbf{C}_T$ is defined as the product of three bell-shaped (Gaussian) covariances, separable in the longitude ϕ, latitude θ, and vertical (terrain-following) s coordinate used in ROMS. For an element of $\mathbf{C}_T$ corresponding to model nodes (ϕ_1, θ_1, s_1) and (ϕ_2, θ_2, s_2),

$$\langle\delta T(\phi_1,\theta_1,s_1)\delta T(\phi_2,\theta_2,s_2)\rangle = \sigma_T(\phi_1,\theta_1,s_1)\sigma_T(\phi_2,\theta_2,s_2)$$
$$\times \exp\left(-\frac{(\phi_1-\phi_2)^2}{2l_\phi^2}\right)\exp\left(-\frac{(\theta_1-\theta_2)^2}{2l_\theta^2}\right)\exp\left(-\frac{(s_1-s_2)^2}{2l_s^2}\right),$$
$$(8)$$

where σ_T is the error standard deviation.

[15] As is always the case in data assimilation, the choice of $\mathbf{C}_0$ is a compromise between physical plausibility, time required to develop the implementation, and computational efficiency. The covariance described above is regarded as a useful starting choice that can possibly be refined based on outcomes of the DA tests.

[16] Here, the following model initial error covariance parameters are chosen. Decorrelation length scales l_ϕ and l_θ for longitude and latitude are chosen to yield a decorrelation scale of approximately 50 km in the horizontal. The vertical scale l_s yields a 50 m vertical decorrelation error scale in a 3000 m water column. For each vertical profile, σ_T is 0.5°C at the surface and is reduced with depth as $\exp(z/z_0)$, where $z_0 = 100$ m (z is 0 at the surface and negative at depth). Thus, the covariance is tuned to provide maximum impact in the upper ocean layers.

4. Observations and Data Functionals

[17] We assimilate the Archiving, Validation, and Interpretation of Satellite Oceanographic data (AVISO) along-track altimetry from Jason, TOPEX, and Envisat (specifically, delayed time, "updated," absolute dynamical topography data, smoothed along each track by the data provider and available at an along-track resolution of 18 km: http://aviso.oceanobs.com; see Figure 4). The assimilation period is 1 June to 10 October 2005. Examples of along-track data coverage provided by the 3 satellites in 6 day assimilation windows are shown in Figure 3.

[18] Attention must be given to how SSH observations from altimetry are interpreted in the DA system. For several reasons (not all listed here), matching mean levels in ROMS to those from altimetry can be nontrivial. For example, ROMS is a Boussinesq model and does not reproduce volume changes associated with thermal expansion, which are present in the altimetry data. These steric signals have
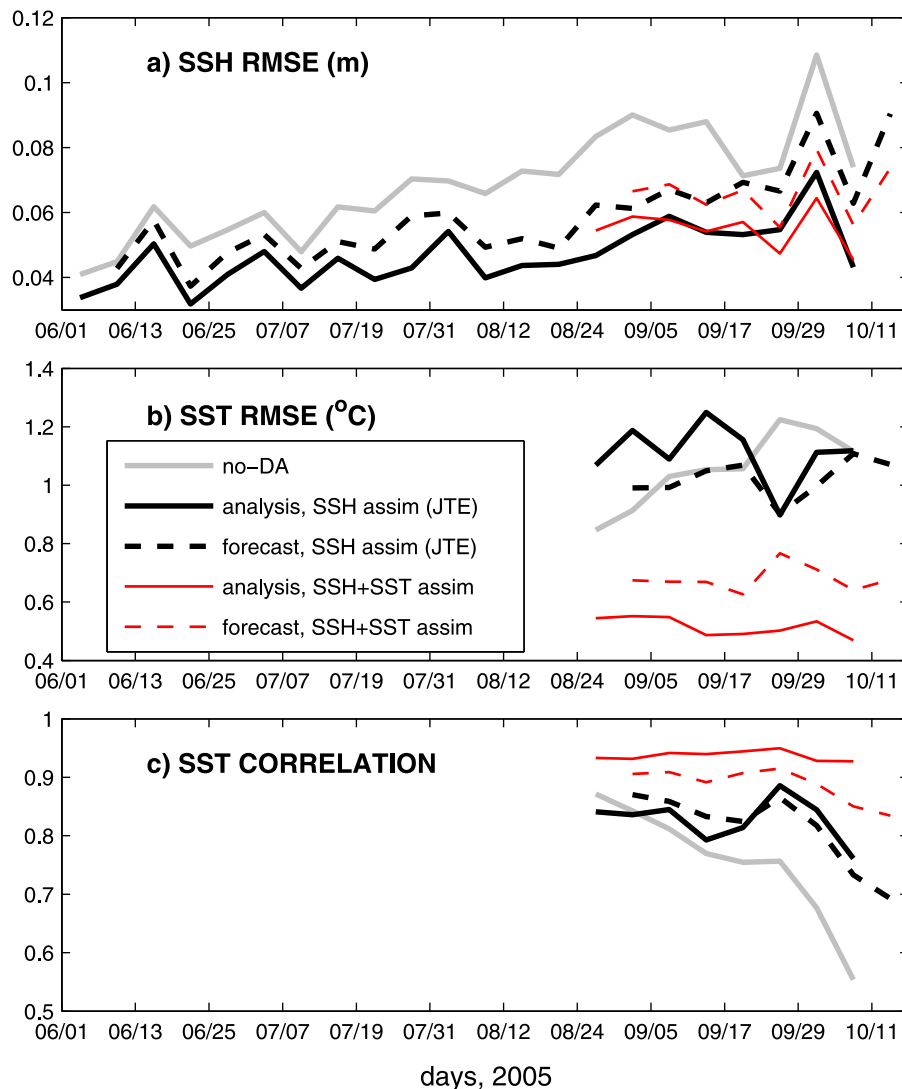
Figure 5. Model-data statistics averaged over the domain area and assimilation window time, comparing cases JTE and JTE-SST: (a) SSH RMSE, using along-track demeaned values (TOPEX, Jason, and Envisat data combined); b) SST RMSE; and c) SST correlation. Lines are for the no DA case (gray), JTE analysis (solid black), JTE forecast (dashed black), JTE-SST analysis (solid red), and JTE-SST forecast (dashed red).

large spatial scales and thus mostly affect the along-track mean within our model domain. Here, we assimilate the dynamically important along-track SSH slope and thus discard information about the along-track mean. The corresponding data penalty term in the cost function is

$$(\mathbf{d} - L\mathbf{u})'\mathbf{C}_d^{-1}(\mathbf{d} - L\mathbf{u}) = \sigma_d^{-2} \sum_{k=1}^{K} \left(\frac{g}{f}\right)^2$$

$$\cdot \left[\frac{\zeta_{2,k}^{obs} - \zeta_{1,k}^{obs}}{\Delta x_k} - \frac{\overline{\zeta_{2,k}^{mod}(t) - \zeta_{1,k}^{mod}(t)}}{\Delta x_k}\right]^2, \ (9)$$

where $\zeta_{1,k}$ and $\zeta_{2,k}$ are model (*mod*) or observed (*obs*) SSH values at the neighboring along-track locations 1 and 2 (their position changes with k), Δx_k is the distance between

these locations, g is gravity, f is the Coriolis parameter, and the overbar denotes time averaging of the model SSH over a 1 day interval centered on the time of measurement (introduced to possibly filter high-frequency signal in the model output). In (9), it is assumed that the data errors are uncorrelated, $\mathbf{C}_d = \sigma_d^2\mathbf{I}$, where $\mathbf{I}$ is the unity matrix. The assumption of uncorrelated data errors is more appropriate for the slope data than original along-track SSH, since the component of error associated with the along-track mean, implying a long decorrelation scale, is removed. Observational locations do not generally coincide with the points of the regular model grid, such that sampling also involves interpolation from the model grid to the observational locations 1 and 2 [not written explicitly in (9)].

[19] Note that (9) defines the following data functional, or sampling rule, matching the model and observed SSH
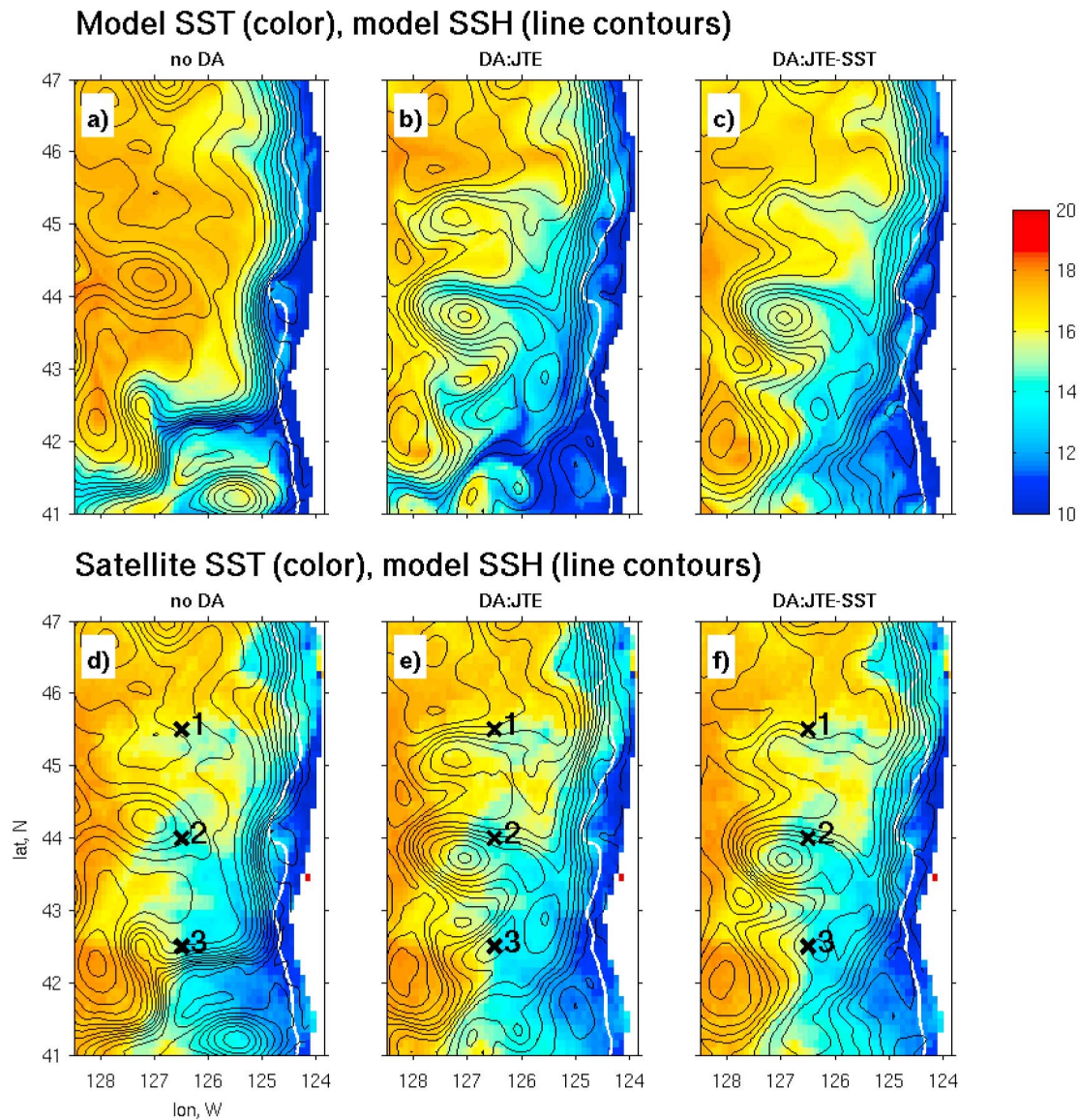
Model SST (color), model SSH (line contours)

Satellite SST (color), model SSH (line contours)

Figure 6. Maps of daily SST (color) and SSH (line contours every 2.5 cm), 28 September 2005: (a–c) model SST and model SSH and (d–f) satellite SST and model SSH (points marked 1, 2, and 3 are explained in text): the no DA (Figures 6a and 6d), JTE (Figures 6b and 6e), and JTE-SST (Figures 6c and 6f) cases. The white contour is the 200 m isobath.

slopes, scaled such that it can be interpreted as the cross-track component of the surface geostrophic current

$$L_k \mathbf{u} = \frac{g}{f} \frac{\overline{\zeta_{2,k}^{mod}(t) - \zeta_{1,k}^{mod}(t)}}{\Delta x_k}. \qquad (10)$$

However, it is important to understand that we do not attempt to match the observed scaled SSH slope to the total model surface velocity, which includes both geostrophic and ageostrophic components. The scaling is introduced for convenience, since we have a better intuition about the error level σ_d in the geostrophic velocity than SSH slope observations.

[20] Multisatellite blended 0.1 degree resolution SST maps from NOAA CoastWatch are utilized for verification of results of SSH assimilation and then for assimilation. This product combines data from the Advanced Microwave Scanning

Radiometer (AMSR-E) instrument, a passive radiance sensor aboard the Aqua spacecraft, Advanced Very High Resolution Radiometer (AVHRR), geostationary GOES Imager, and Moderate Resolution Imaging Spectrometer (MODIS). These composites are available daily and represent weighted averages over 5 days. In our applications they have been compared to daily averaged model fields. In June–July 2005, these maps are strongly affected by noise from the GOES images. Later in our study period, a continuous series of the composite images apparently free of this problem are available from mid-August to October. Thus, only SST data between 24 August and 10 October are used for quantitative model-data comparisons and assimilation.

[21] For the geostrophic velocities estimated from the smoothed along-track altimetry, the error standard deviation of $\sigma_{d,SSH} = 0.05$ m s^{-1} is assumed; for SST, $\sigma_{d,SST} = 3°$C.
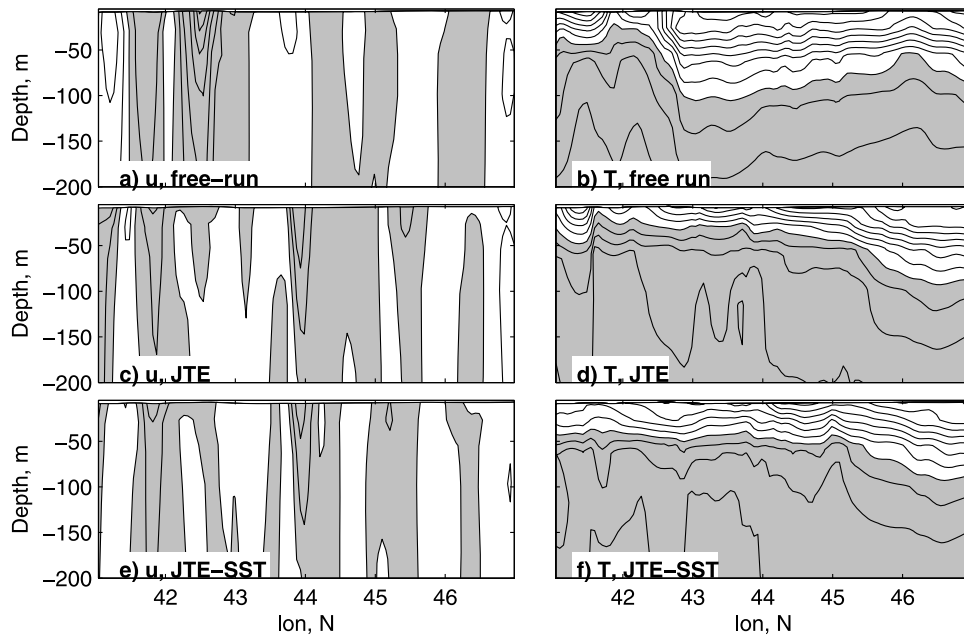
Figure 7. Meridional sections of daily averaged (a, c, and e) u and (b, d, and f) T at 126°W, 28 September 2005: free run model (Figures 7a and 7b) and JTE (Figures 7c and 7d) and JTE-SST (Figures 7e and 7f) cases. In u plots, the contour interval is 0.1 m s^{-1}, with negative values shaded. In T plots, the contour interval is 1°C, with values ≤10°C shaded.

These values have been chosen based on a series of sensitivity experiments, to yield the best overall performance in terms of both SSH and SST. The data error variance $\sigma_{d,SSH}^2$ is comparable to the expected prior model error variance in the sampled scaled SSH slope. The latter can be estimated as the representer function corresponding to this observation sampled at the observation location/time, $L_k \mathbf{r}_k$ (see Appendix A). Using the representers that were computed directly (these are used to precondition the iterative minimization), the average expected model error variance is $(0.025 \text{ m s}^{-1})^2$. Note this estimate depends on the assumed $\mathbf{C}_0$.

[22] Although data error $\sigma_{d,SST}$ chosen seems high, this may reflect the fact that the SST data are assimilated daily, but are actually a result of (weighted) averaging over a larger time interval (5 days). The situation is similar to the following simple example. If an n day average observation $\overline{T}^{obs}$ is available, an appropriate form of the data penalty term should be

$$J_1 = \sigma_1^{-2} \left(\overline{T}^{obs} - \frac{1}{n} \sum_{i=1}^{n} T_i^{mod} \right)^2, \qquad (11)$$

where T_i^{mod} is the model value averaged over day i. However, instead of matching the n day model and data averages as in (11), we have chosen to assimilate the same observation on each day (this simplifies implementation in the short assimilation windows used)

$$J_2 = \sigma_2^{-2} \sum_{i=1}^{n} \left(\overline{T}^{obs} - T_i^{mod} \right)^2. \qquad (12)$$

The simplified form J_2 will be equivalent to J_1 under the following assumptions: (a) the model solution is changing slowly such that $T_i^{mod} \approx (1/n) \sum_{i=1}^{n} T_i^{mod}$, and (b) $\sigma_2 = \sigma_1 \sqrt{n}$.

If the simplified form (12) is chosen instead of the more appropriate (11), then the error value σ_1 should be increased by the factor of $\sqrt{n}$.

5. Assimilation Results

[23] Two experiments are discussed here. In case JTE, we assimilate along-track altimetry from Jason, TOPEX, and Envisat. In case JTE-SST, SST information is assimilated in addition to data from the three altimeters. In both cases, the data errors are assumed to be uncorrelated (i.e., $\mathbf{C}_d$ is diagonal).

5.1. Area-Averaged Model-Data Statistics

[24] Figure 5a shows time series of the SSH root-mean-square model-data difference (or RMS error (RMSE)) averaged over the domain and each 6 day time interval, for the free run model ("no DA", gray), a series of 6 day JTE analyses (solid black), and 6 day JTE forecasts (dashed black). To compute RMSE in each 6 day window, the SSH data and correspondingly sampled model fields were demeaned along each track. The use of AVRORA to correct initial conditions results in a better fit of the nonlinear ROMS analysis solutions to the data (smaller RMSE), increasing our confidence that the AVRORA codes are dynamically consistent with ROMS. Improvement in the accuracy of 6 day forecasts, compared to the free run model, suggests that the assimilation scheme developed can be useful for short-term forecasting of the near-surface quasi-geostrophic circulation over the slope and in the CTZ. SSH RMSE for all cases increases toward the end of the upwelling season as the CTZ jets and eddies become more energetic.

[25] For case JTE, fits to unassimilated SST data are shown in Figure 5b, where area- and 6 day-averaged SST
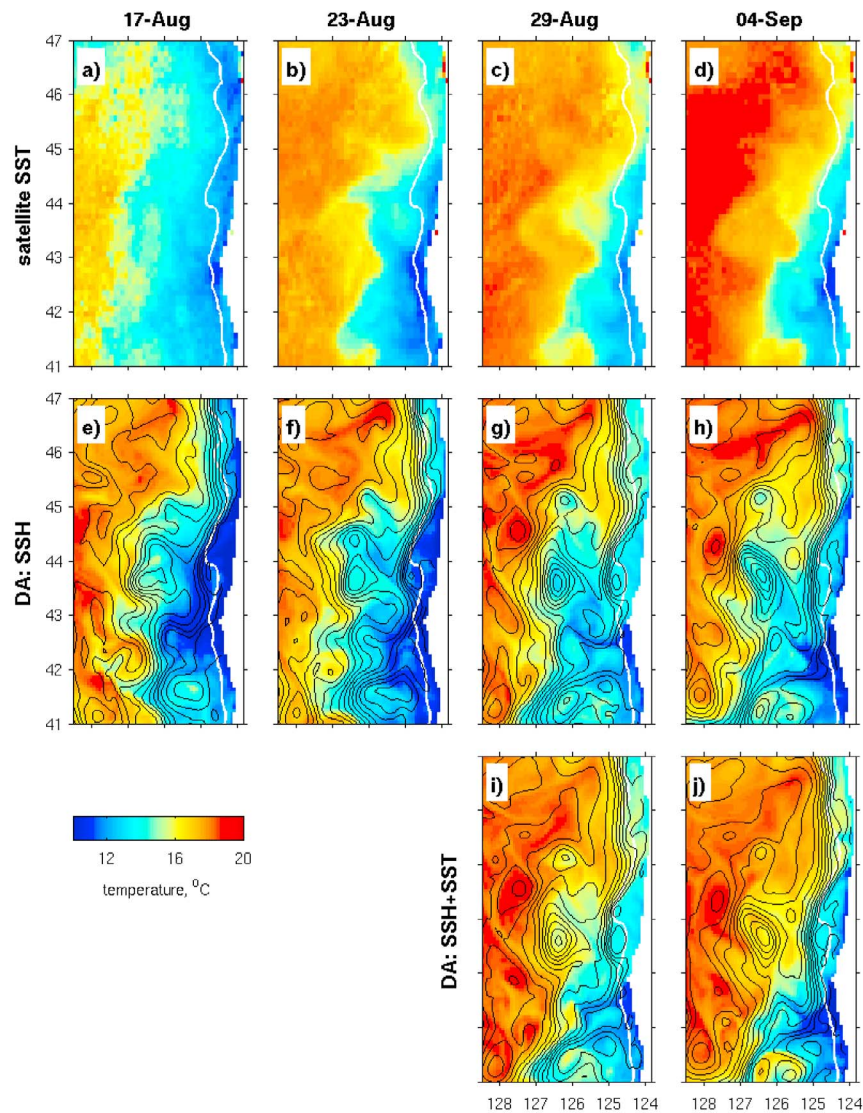
Figure 8. Maps of daily SST (color) and SSH (line contours every 2.5 cm) on selected dates, 17 August to 28 September 2005: (a–d and k–n) satellite SST, (e–h and o–r) SST and SSH from JTE, and (i, j, and s–v) SST and SSH from JTE-SST.

RMSE are plotted. Corresponding model-data correlation coefficients are shown in Figure 5c. For case JTE, the analysis and forecast SST RMSE are at the same level as the no DA case. At the same time, the analysis and forecast SST model-data correlations in August–October are significantly higher.

[26] Assimilation of SST in addition to SSH (case JTE-SST; red lines in Figure 5) improves the fit to SST for both analyses and forecasts, resulting in lower SST RMSE and higher correlation than the no DA and JTE cases. It also provides moderate improvement to the SSH RMSE at the end of the assimilation period, compared to case JTE. The SSH and SST data assimilated in our system thus complement each other, rather than conflict.

5.2. Assimilation Effect on the Surface Fields

[27] Improvement of the SST model-data correlation (but not necessarily RMSE) resulting from the along-track SSH

assimilation is associated with improved geometry of the SST cold upwelling front. To demonstrate this, daily averaged (28 September) surface maps of model SSH (line contours) and model SST (color) are shown in Figures 6a–6c, where plots from the left to the right correspond to the no DA, JTE, and JTE-SST cases. In both DA cases, analyses for day 6 are plotted. For comparison, in Figures 6d–6f the *satellite* SST composite corresponding to the same day is repeated three times, overlain by the *model* SSH contours from the three cases. Markers 1, 2, and 3 (see Figures 6d–6f) point to the areas of colder observed SST, potentially associated with jets separated from the shelf in the CTZ. By the end of September, the free run model SST (Figure 6a) is qualitatively very different from the observed field (Figure 6d). In particular, no cold water separation is found in the free run model at the locations corresponding to markers 1 and 2. In area 3 (off Cape Blanco, 42.3°N), the free run model shows separation as a narrow jet, while satellite SST suggests
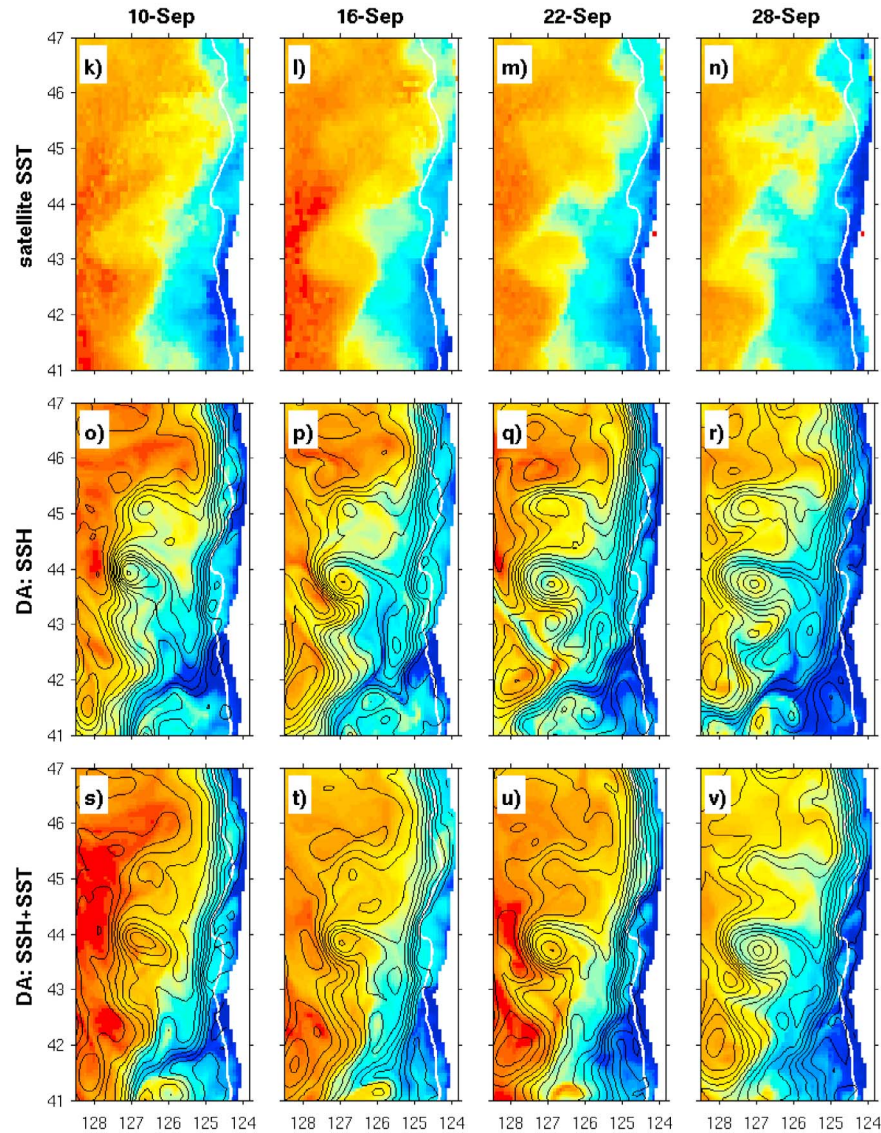
Figure 8. (continued)

a more diffused flow. In case JTE, contours of SSH (surface geostrophic current stream function) are modified such that all the three separation areas become apparent, connected with the shelf current (Figure 6e). The observed SST is more comparable to the JTE analysis (cf. Figures 6b and 6e) than the free run case (Figure 6a). Assimilation of SST in addition to SSH (Figures 6c and 6f) modifies details of the predicted surface geostrophic currents, but does not affect the qualitative character of the flow.

[28] Assimilation affects not only surface, but also subsurface fields. Figure 7 shows vertical sections of the daily averaged (28 September) zonal current u and potential temperature T along longitude 126°W. The energetic jet found in the free run model between 43°N and 44°N is replaced in the DA runs with several weaker offshore jets. In the temperature sections, the thermocline between 43°N and 45°N is shallower in the DA solutions than in the free run model, as discussed in more detail below.

5.3. The Outer Front

[29] Results of SSH assimilation suggest that an outer front is formed in the CTZ in August 2005, in addition to the front associated with the shelf current. The outer front is seen, e.g., in Figures 6b and 6c in the area south of 46°N, associated with a continuous southward geostrophic current meandering between longitudes 126°W–128°W. This front is not reproduced in the free run model (Figure 6a) and may not be easily identified in the satellite data (because of sparse SSH coverage and the sometimes relatively weak contrast in SST).

[30] The evolution of this front is explained in Figure 8, where SST and SSH maps for 16 August to 28 September are plotted. Each column of plots corresponds to the last day of analysis in a sequence of assimilation windows. Plots of satellite SST are in the top row, model SSH and SST (case JTE) in the middle, and model SSH and SST (JTE-SST) in the bottom row. As a result of the sustained upwelling
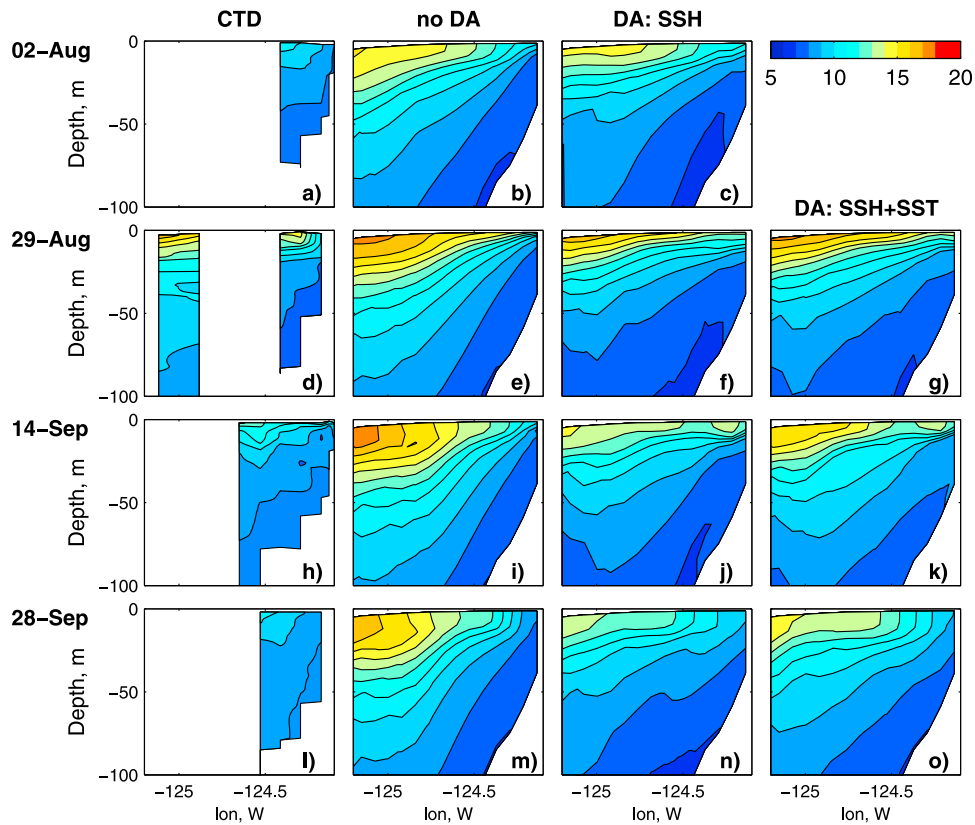
Figure 9. Observed CTD and modeled daily averaged potential temperature sections at 44.65°N. Each row corresponds to a day of 2005 as marked: (a, d, h, and l) observations, (b, e, i, and m) free run model (no DA), (c, f, j, and n) JTE, and (g, k, and o) JTE-SST. The contour interval is 1°C.

favorable wind conditions in the first two weeks of August (see Figure 2), widespread offshore near-surface transport of colder waters occurs, e.g., apparent both in the satellite SST and case JTE on 17 August (see Figures 8a and 8e). On this day, SSH contours show an intensified surface geostrophic current along the cold SST front at 127°W. In the following weeks (e.g., 23 August to 22 September), during a period of a relatively weaker wind, that southward current maintains its presence along 127°W. At the same time, satellite SST data suggest that the area between the outer front and the shelf jet warms up near the surface and the large temperature contrast across the outer front fades (though a weak, 2°C–3°C contrast can still be identified if the color scale is adjusted). The warming of the surface water inshore of this current is also reproduced in the JTE solution, but is weaker than in the observed SST. Combined SSH-SST assimilation (Figures 8i, 8j, and 8s–8v) helps to constrain SST in this area, modifying SSH contours compared to case JTE, but not destroying the outer front.

[31] To provide a full description of the structure of the outer front, it would be desirable to compare modeled and observed vertical hydrographic sections across the front. Unfortunately, such data could not be found. However, the effect of this front affects the hydrographic structure closer to the coast, where vertical section data are available for comparison. At 45.65°N, conductivity-temperature-depth (CTD) cross-shore transects obtained over the shelf and continental slope (courtesy of W. Peterson and J. Peterson,

NOAA Northwest Fisheries Science Center) are compared to the modeled temperature sections (Figure 9). The observed section on 29 August extends farthest offshore. On this day, the depth of the thermocline in the model run without DA is considerably larger than in the observations. In the practice of modeling this may casually be explained as the result of insufficient vertical resolution and associated model diffusion. However, quite surprisingly, we find that in both assimilation cases, JTE and JTE-SST, the depth of the thermocline over the continental slope is smaller than in the no DA case and is much more comparable to the observations. In Figure 10 the model sections are extended westward to 128.5°W and both temperature and meridional velocities are shown for 29 August and 14 September. These sections suggest that the relatively thinner thermocline in the CTZ is associated with the outer front, present in the DA solutions near 127°W. The frontal current is vertically sheared and, by thermal wind balance, a strong horizontal density (and temperature) gradient is present across the front. Isotherms on the inshore side of the outer front are uplifted, compared to the offshore side, and this hydrographic condition extends all the way to the continental slope. We further hypothesize that this uplifting can cause stronger near-surface stratification in the area between the outer front and shelf limiting the downward turbulent flux of heat and providing conditions for rapid warming of the surface waters, observed at the end of August. Because of the limited model vertical resolution in this area, the surface layer does not warm up as quickly in
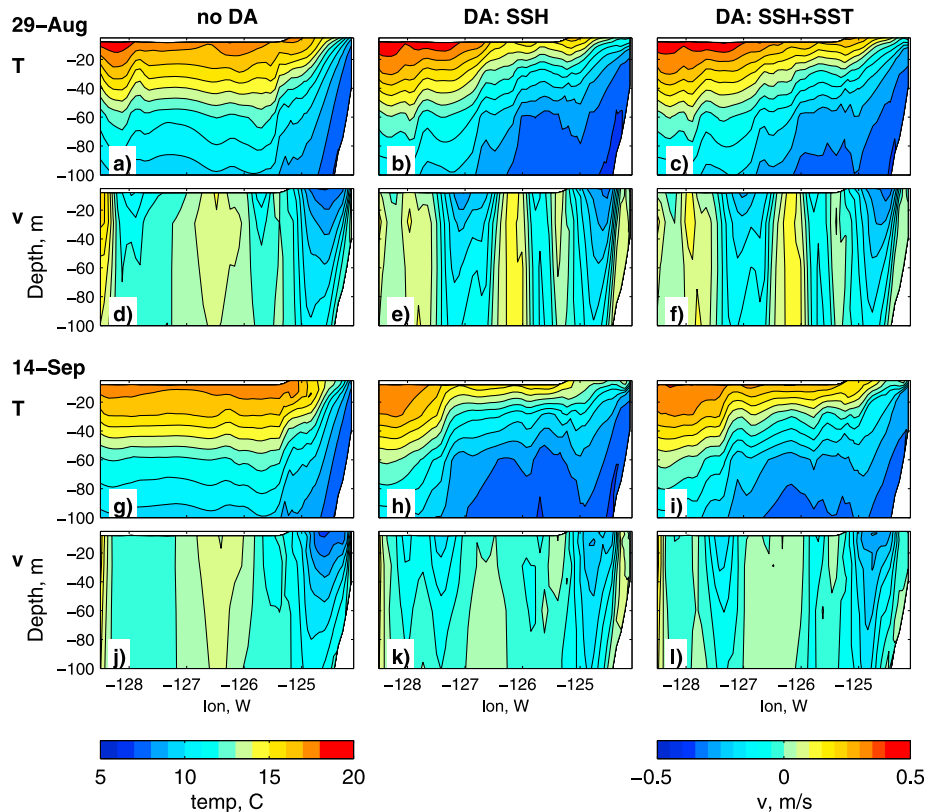
Figure 10. Model potential temperature T and meridional velocity v sections at 44.65°N, extended to 128.5°W, (a–f) 29 August 2005 and (g–l) 14 September 2005: no DA (Figures 10a, 10d, 10g, and 10j), JTE (Figures 10b, 10e, 10h, and 10k), and JTE-SSH (Figures 10c, 10f, 10j, and 10l). The contour interval is 1°C and 5 cm s^{-1} for T and v, respectively.

our DA cases. More detailed analysis of this effect would be possible with a higher-resolution model, left as a topic of future studies.

5.4. The Heat Equation Term Balance Analysis

[32] DA improvements in the near-surface temperature can result in part from the corrected advection of T. Also, heat is introduced or removed from the system when an instantaneous DA correction to T is made at the beginning of each analysis window. This correction is not easy to associate with any physical mechanism. However, we can at least evaluate its relative magnitude, e.g., compared to other terms in the heat equation, and its net effect for a coastal control volume.

[33] For this study, we compute terms in the heat equation integrated vertically over the entire water depth and horizontally over the subdomain shown as a gray box in Figure 1, which extends south to north between 41°N and 47°N and east to west between the coast and 126°W, including both the shelf and a part of the CTZ. The heat equation integrated over the specified control volume V is

$$c_p\rho_\circ \frac{d}{dt}\int_V T\, dV = -c_p\rho_\circ \int_B T\mathbf{u}\cdot\mathbf{n}\, dB + \int_A Q_{atm}\, dA$$
$$+ c_p\rho_\circ \sum_k \delta(t-t_k)\int_V \delta T_k\, dV, \qquad (13)$$

where T is the temperature from the DA analysis, $c_p = 3985$ J kg^{-1} K^{-1} the specific heat at constant pressure, $\rho_\circ$ the

reference density, B the vertical boundary of the control volume, $\mathbf{u} = (u, v)$ the horizontal current vector, $\mathbf{n}$ the outgoing normal unit vector, A the surface area, Q_{atm} the net atmospheric heat flux into the ocean, and δT_k the DA correction applied at time t_k. The term on the left-hand side of (13) is the tendency in the volume-integrated heat content. Terms on the right-hand side of the this equation include (left to right) the net advective heat flux through the open ocean boundaries, the atmospheric heat flux, and the DA correction term. The latter is written as a series of impulsive (δ function type) corrections at the beginning of each analysis interval. The horizontal diffusion term is small and is neglected in (13). For analysis, the terms will be divided by the surface area A to obtain units of W m^{-2}.

[34] The time series of 4 h time-averaged heat balance terms for the free run model ($\delta T_k = 0$) are shown in Figure 11a. Positive values for every term correspond to warming conditions. Throughout the study period (June–September) both the atmospheric flux and horizontal advective flux are significant contributors to the heat budget in the chosen area. Temporal variability in the tendency term is dominated by the horizontal advective flux, which mostly provides cooling of the selected control volume.

[35] To show the relative contribution of the DA correction term, we compute series of 6 day time-averaged terms, such that each averaging interval is centered at the time of the DA correction (in other words, each averaging window includes 3 days from the current and 3 days from the
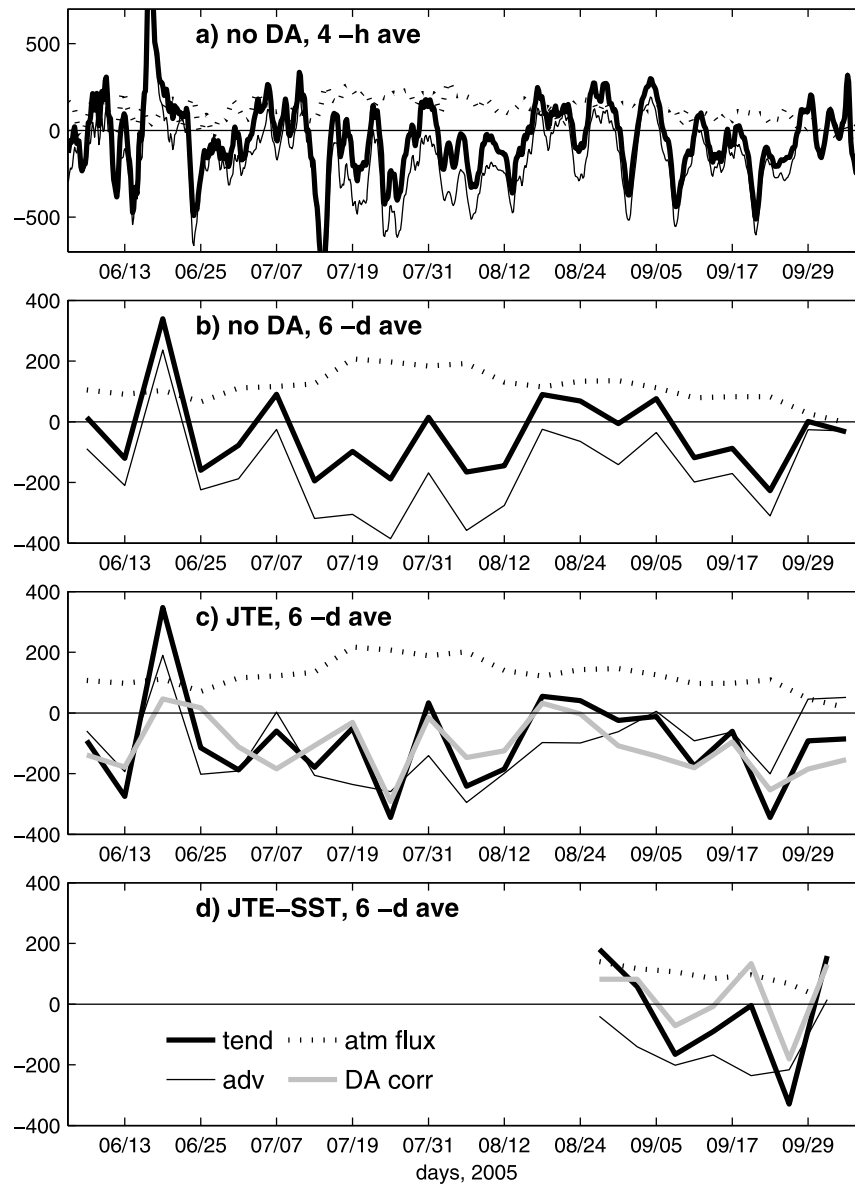
Figure 11. Depth-integrated, area-averaged terms (W m^{-2}) in the heat equation (tendency, advection, atmospheric heat flux, and DA correction terms shown as thick solid black, thin solid black, dotted, and gray lines, respectively) for the coastal ocean control volume shown as a box in Figure 1: (a) free run model, 4 h averages; (b) free run model, 6 day averages; (c) case JTE, 6 day averages; and (d) case JTE-SST, 6 day averages.

previous assimilation window). In particular, for a given interval ($t_{(-3d)}$, $t_{(+3d)}$), the tendency term is computed as

$$\text{Tend} = \frac{c_p \rho_\circ}{t_{(+3d)} - t_{(-3d)}} \int_V \left(T_{(+3d)} - T_{(-3d)}\right) dV, \quad (14)$$

where $T_{(+3d)}$ and $T_{(-3d)}$ are temperature values at the ends of the averaging interval. For the same interval, the DA correction term is

$$\text{DA corr} = \frac{c_p \rho_\circ}{t_{(+3d)} - t_{(-3d)}} \int_V \left(T_{(0^+)} - T_{(0^-)}\right) dV, \quad (15)$$

where $T_{(0^-)}$ and $T_{(0^+)}$ refer to the temperature values at the middle of the averaging interval before and after the cor-

rection is made, respectively. The series of the 6 day averaged terms are shown in Figures 11b, 11c, and 11d, for the free run, JTE, and JTE-SST cases, respectively. In case JTE, we find that the DA correction term is of the same order of magnitude as other terms. On average, it provides cooling of the volume. Variability in the net heat flux through the side boundaries is qualitatively similar to that in the free run model, although its magnitude is smaller in case JTE. Variability in the tendency term is qualitatively similar to that in the no-DA case. In case JTE-SST, we note that variability in the DA correction term in August–October is centered more closely around 0 (this term averaged between 27 August and 4 October is 24 W m^{-2} in case JTE-SST and −160 W m^{-2} in case JTE). These analyses suggest that in
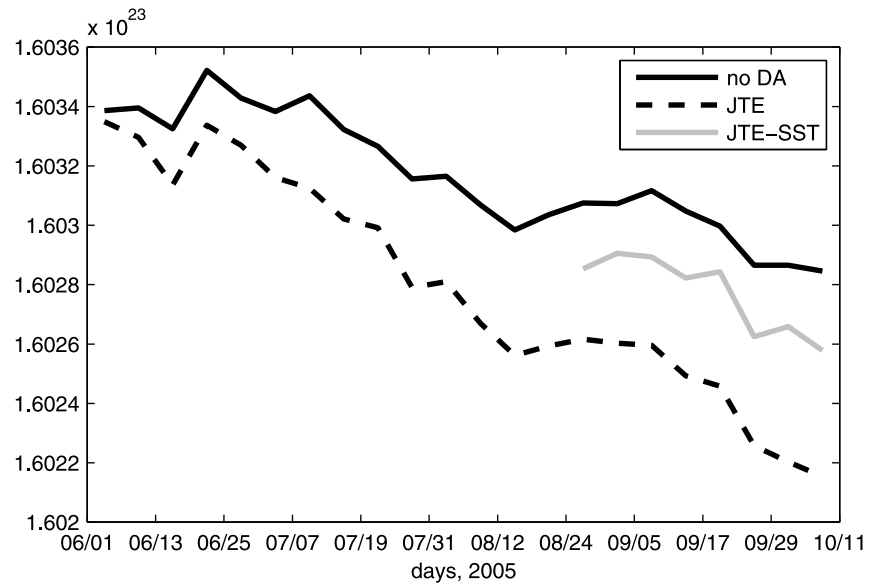
Figure 12. Time series of the ocean heat content (J) integrated over the coastal control volume shown as a gray box in Figure 1.
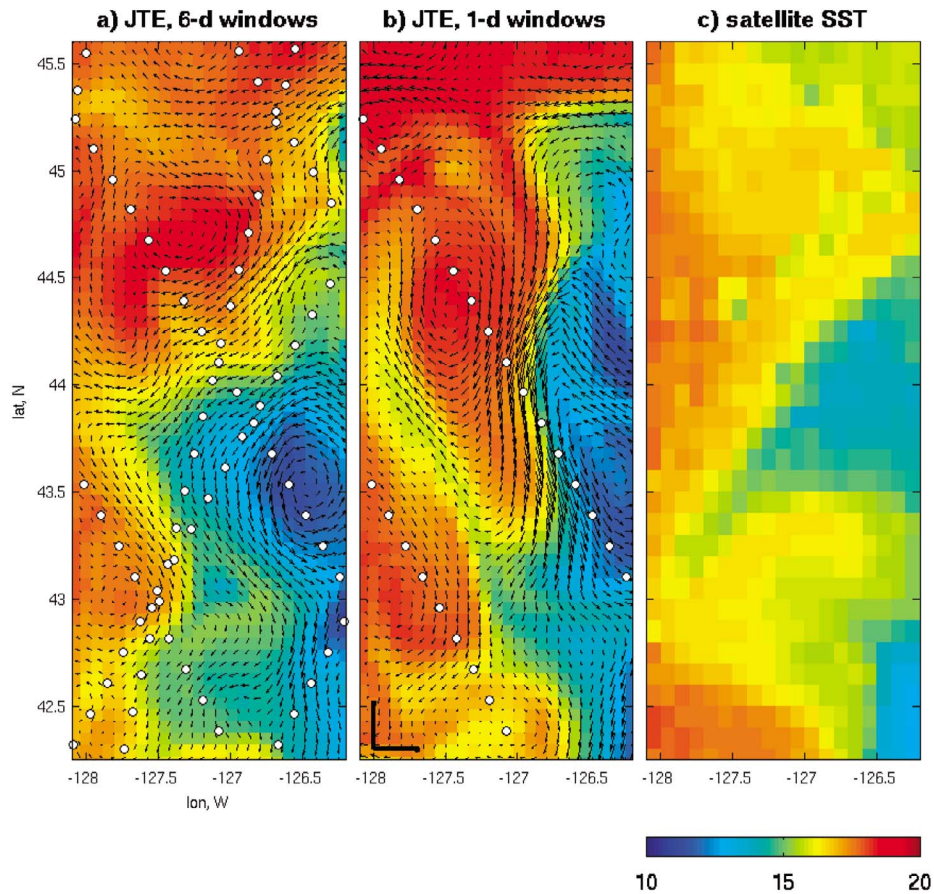

Figure 13. Model SST and surface velocity snapshots, 24 August, 0000 UTC: (a) JTE (assimilation in 6 day windows) and (b) JTE-1d (assimilation in 1 day windows). White circles show altimetry tracks assimilated in respective windows. Scale vectors (bold) are 1 m s^{-1}. Figures 13a and 13b are initial conditions in their respective analysis windows. (c) Multisatellite blended SST (5 day weighted average, centered on 24 August).
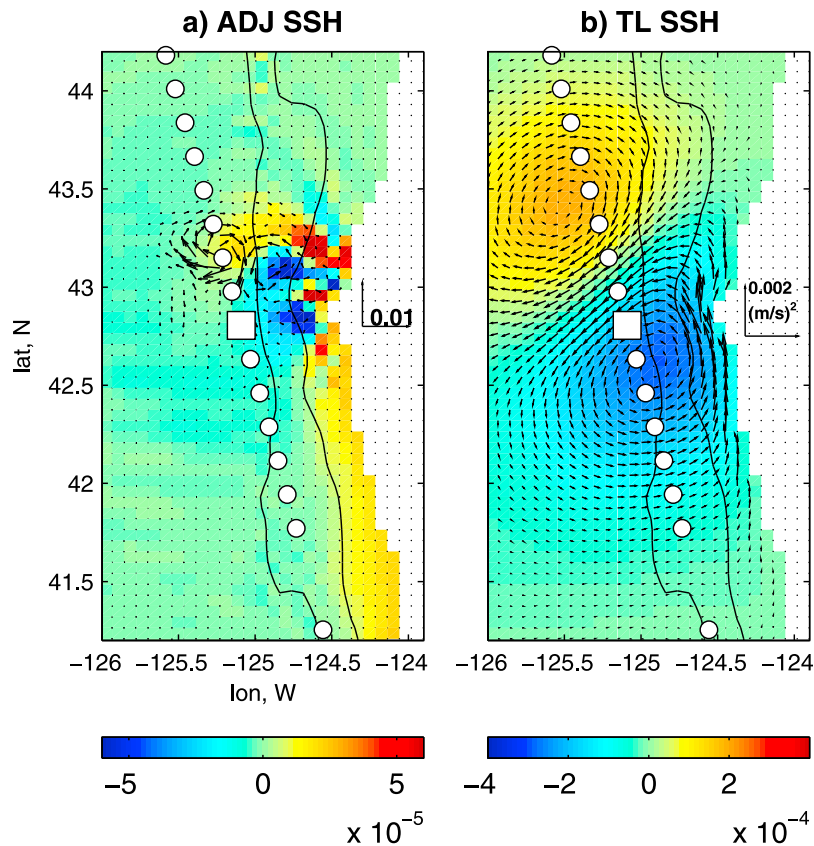
Figure 14. The SSH components of the adjoint representer solution $\lambda_k(0)$ and representer $r_k(0) = C_0\lambda_k(0)$, shown at $t = 0$, corresponding to the observation of the scaled along-track SSH slope taken at $t_{obs} = 3.2$ days: (a) adjoint SSH (color, s^{-1}) and velocity (vectors) and (b) representer SSH (color, m^2 s^{-1}) and velocity. Circles denote the track, and the square denotes the observation location. Contours are bathymetry (200 and 1000 m). The background solution is the JTE forecast, 24–29 August 2005.

case JTE, the multivariate covariance C_0 may yield too strong cooling inshore of the CTZ front. Assimilation of SST in addition to SSH mitigates this effect.

[36] Figure 12 shows the time series of the total ocean heat content integrated over the control volume (units are Joules), for the no DA, JTE, and JTE-SST cases. It is computed as

$$Q(t) = \rho_\circ c_P \int_V T_{(K)} \, dV, \qquad (16)$$

where $T_{(K)}$ is the potential temperature in Kelvin units. The values have been computed using analyses at the middle of each assimilation window. Despite the positive atmospheric heat flux, the volume is cooling over the chosen study period (June-October), as has already been suggested by the predominantly negative sign of the tendency. Case JTE constrained by assimilation of along-track SSH probably overestimates the volume cooling. The trend in the JTE-SST curve is closer to the no DA case.

6. Discussion

[37] In this section we describe complementary analyses that can potentially demonstrate value, as well as limitations, of our approach and point to directions for future research.

[38] We have shown that variational (4DVar-type) assimilation of the along-track SSH slope helps to improve geometry of the SST front. Could a similar result be obtained using a simpler DA method? In 3DVar [*Li et al.*, 2008] or optimal interpolation [*Oke et al.*, 2002; *Kurapov et al.*, 2005a, 2005b, 2005c], one would bin the data at the end of an analysis interval and provide instantaneous correction utilizing a forecast error covariance that does not change from cycle to cycle. With such an approach, no adjoint model is necessary since observational information is not propagated back in time. The analysis intervals would be much shorter (e.g., a few hours). Since development of a 3DVar system is still a tedious task, we do not provide a direct performance comparison to the variational methods used here. However, if our variational system is utilized in a series of very short windows, the result should be closer to 3DVar. An additional experiment (JTE-1d) has been run in a series of 1 day windows assimilating SSH slope alone. This case yielded results similar to case JTE in terms of area-averaged model-data statistics discussed in Figure 5 (including improvement of the SST model-data correlation), suggesting that 3DVar assimilation of the SSH slope may also provide a useful constraint on the SST front geometry.

[39] However, despite the similarity in area-averaged model-data statistics, details of the modeled SST fronts obtained in the two cases differ. Figures 13a and 13b show
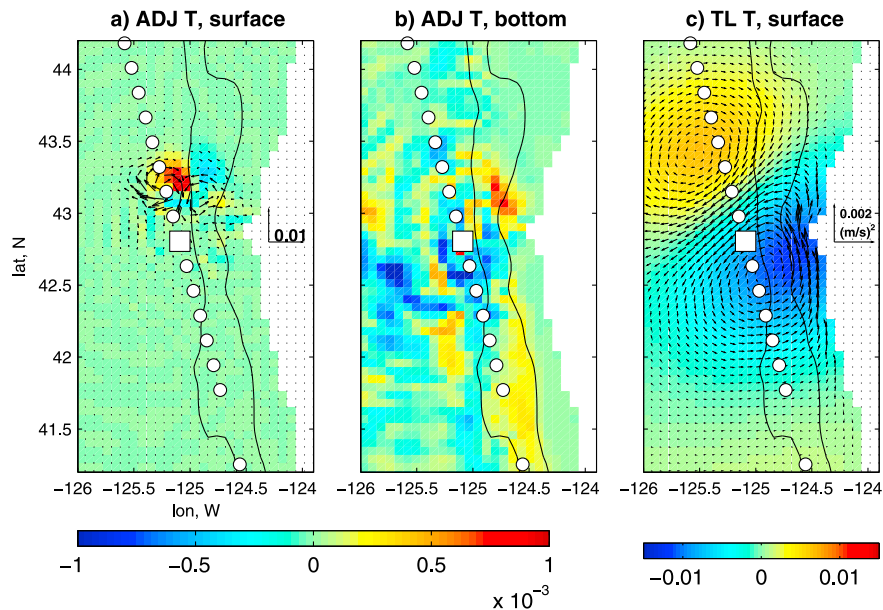
Figure 15. The T components of the adjoint representer solution $\boldsymbol{\lambda}_k(0)$ and representer $\mathbf{r}_k(0) = \mathbf{C}_0\boldsymbol{\lambda}_k(0)$, shown at $t = 0$, corresponding to the observation of the scaled along-track SSH slope taken at $t_{obs} = 3.2$ days: (a) adjoint surface T (color, m s^{-1} °C^{-1}) and velocity (vectors), (b) adjoint bottom T (same color scale as Figure 15a), and (c) representer fields of surface T (color, m s^{-1} °C) and surface velocity (vectors). Circles denote the track, and the square denotes the observation location. Contours are bathymetry (200 and 1000 m).

snapshots of the analysis SST and surface velocities zoomed on a frontal area on 24 August 2005, 0000 UTC, for cases JTE and JTE-1d. Both states are initial conditions for analysis runs in their respective windows. The front structure in case JTE (Figure 13a) is constrained by assimilation of SSH slope from several intersecting tracks available in the 6 day window (shown as white circles) and potentially provides a more accurate (and stable with respect to data errors) estimate of the surface currents than case JTE-1d (Figure 13b), in which time interpolation between tracks on different days is not done. If the SSH slope data are overfit, the resulting surface velocities and the cross-front SST contrast can be too large, as is potentially the case in Figure 13b. Also note that the orientation of the SST front (northeast to southwest between 43.5°N and 45°N) in case JTE is qualitatively more comparable to the observed SST (Figure 13c) than in case JTE-1d.

[40] Ability to propagate observational information back in time is one of potential advantages of variational DA. The effect of dynamics on information propagation can be seen in the adjoint representer solution at initial time $\boldsymbol{\lambda}_k(0)$, obtained as a result of the adjoint model run forced by the sampling function $\mathbf{q}_k(t)$ corresponding to a single observation (see (3) and Appendix A). Note that the adjoint solution shows model sensitivity of the sampled quantity to all initial condition fields and is thus a multivariate field (which consists in our case of SSH, u, v, T, and S components). The units of each adjoint component are determined as [units of the sampled quantity] × [units of the adjoint solution component]$^{-1}$. Based on the statistical theory [*Bennett*, 2002], $\boldsymbol{\lambda}_k(0)$ can be interpreted as the time lag model error covariance of the observed quantity (at $t = t_{obs}$) and all elements of the multivariate model state at $t = 0$, assuming initial errors are not

correlated ($\mathbf{C}_0 = \mathbf{I}$). Figure 14a shows the SSH component of the adjoint solution $\boldsymbol{\lambda}_k(0)$ corresponding to the observation of the scaled along-track SSH slope (cross-track geostrophic velocity component) taken at a location on the continental slope at $t_{obs} = 3.2$ days (here, $t = 0$ corresponds to the beginning of the 6 day analysis window of 24–29 August). This plot reveals effects of advection and coastally trapped waves. The data location is on the path of the background current that was separated from the coast in the CTZ (e.g., see Figure 6b). Due to advection by this current, the area of maximum observation impact at $t = 0$ is found upstream of the observation location, closer to the coast. In that area, both SSH and surface velocity components of the adjoint solution have a dipole structure (which could be expected since the observation tends to impact the model SSH slope without changing the mean level). The signature of coastally trapped waves is found south of the observation location, extending all the way along the slope to the cross-shore boundary, consistent with the analytical representer solution for an idealized coastal model [*Kurapov et al.*, 1999, 2002]. The temperature component of the adjoint solution does not show the effect of coastally trapped waves on the surface (Figure 15a), although this effect is apparent near the bottom (Figure 15b). Additionally, the adjoint solution shows small-scale features associated with inertia-gravity waves, particularly apparent in the bottom T plot.

[41] Implementation of the geostrophically balanced covariance $\mathbf{C}_0\boldsymbol{\lambda}_k(0)$, providing initial conditions for the representer, removes not only the small-scale features, but also the signal associated with coastal trapped waves (which are geostrophic only in the cross-shore direction [*Brink*, 1991]) (Figures 14b and 15c). To preserve the CTW signal in the initial conditions for the TL computation, $\mathbf{C}_0$ must
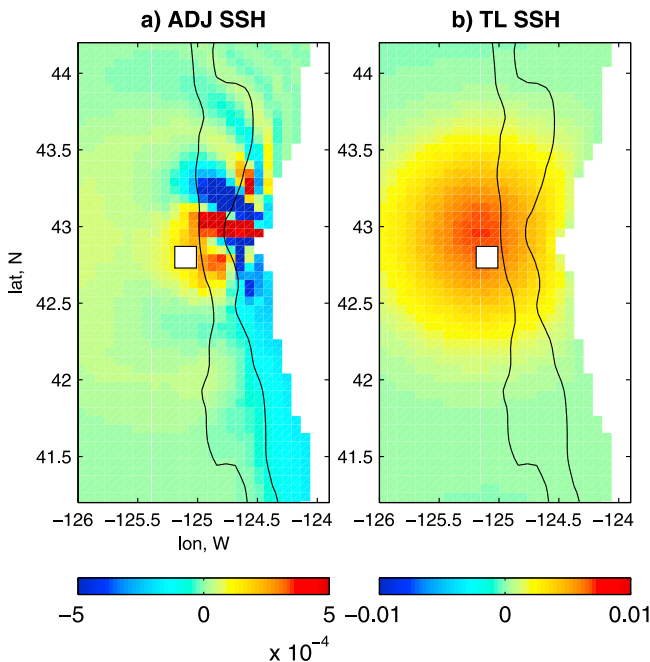
Figure 16. The SSH components of the adjoint representer solution $\boldsymbol{\lambda}_k(0)$ and representer $\mathbf{r}_k(0) = \mathbf{C}_0\boldsymbol{\lambda}_k(0)$, shown at $t = 0$, corresponding to the observation of T (daily averaged value on day 3): (a) adjoint SSH (m^{-1} °C) and (b) representer SSH (m °C). Contours are bathymetry (200 and 1000 m). The background solution is the JTE forecast, 24–29 August 2005.

be modified. Although our implementation does not correct boundary conditions, this study suggests that observations on the slope contain information to constrain those. Correction of the boundary conditions in a 3-D baroclinic problem remains a nontrivial task because of the inherent ill-posed nature of a dynamical problem based on continuous 3-D primitive equations with hydrostatic approximation [*Oliger and Sundström*, 1978].

[42] Analyses of adjoint solutions and representers show that different data types provide different impacts on the model correction. For example, Figure 16 shows the initial adjoint and representer SSH fields corresponding to surface T observation, which can be compared to the fields corresponding to the SSH slope observation at approximately the same location and time (see Figure 14). In particular, the initial representer SSH field corresponding to the T observation has a monopole structure. The positive T correction in the impacted area is associated with the increased SSH and an anticyclonic eddy around the observation location.

7. Summary

[43] Assimilation of along-track satellite SSH in the recently developed AVRORA system, used in combination with the nonlinear ROMS, improves the modeled structure of near-surface geostrophic currents and the coastal SST front associated with summer upwelling off Oregon. In particular, the area-averaged model-data SST correlation is improved as a result of SSH assimilation. Assimilation of SST in addition to SSH further constrains SST and improves the model forecast RMSE for both SSH and SST.

[44] The AVRORA assimilation system allows us flexibility in the choice of the data functionals which match model outputs and observations. By assimilation of along-track slope, rather than SSH, the issue of compatibility of the observed and model mean levels is avoided. The along-track altimetry data provide information about jets and eddies over the continental slope and in the CTZ on spatial scales smaller than the distance between neighboring tracks. In this regard, the DA system can be viewed as an effective, dynamically consistent tool for mapping of the SSH and surface currents using sparse along-track altimetry data.

[45] Variational data assimilation offers many advantages. In terms of CPU time, implementation of the indirect representer method with preconditioning is economical enough to allow running the application described in near-real time, to improve accuracy of initial conditions for operational forecasts in the coastal ocean. The observations do not have to be binned at the end of every analysis window as in sequential methods; instead, they provide a constraint on the model dynamics at the actual time of measurement. Time-averaged or time-filtered information can be conveniently assimilated. Time-space interpolation of sparse and diverse data sets yields accurate and stable estimates of the ocean state.

[46] In our analyses, we touched on the topic of heat balance in the coastal ocean. It would be interesting to extend this analysis to multiyear simulations, using a model of a larger alongshore extent, to understand the seasonal cycle and interannual variability of the heat balance in the coastal ocean and the role of the coastal ocean upwelling systems in the transport of heat and material on larger scales. In longer-time experiments, e.g., reanalyses for studies of climate variability, the amount of heat removed or added by means of DA must be diagnosed. Present results indicate that inclusion of SST in assimilation in addition to SSH reduces bias in the DA correction to the heat equation.

[47] The finding that assimilation of surface satellite data can improve the structure of the near-surface stratification in the CTZ and over the slope was not entirely anticipated, but welcome. It reveals that the currents in the CTZ, at a distance of 200 km from the coast are related to the ocean dynamics all the way to the coast. The shelf, slope, and CTZ present a single, complicated, multiscale system that requires careful study using future observational, modeling, and assimilation efforts.

Appendix A: Elements of the Representer Theory

[48] Using notation introduced in section 3, the representer $\mathbf{r}_k(t)$ is a multivariate time-varying vector that shows zones of influence of a given observation on all components of the ocean state (SSH, velocities, T and S). The observation is defined by the kernel $\mathbf{q}_k(t)$ of the data functional L_k (3). In the case where only initial conditions are corrected, to compute a representer, the ADJ system is run backward in time, forced by $\mathbf{q}_k(t)$, then the adjoint solution is smoothed/filtered at the initial time using $\mathbf{C}_0$, and finally the tangent linear model is run using the filtered initial conditions. The corresponding ADJ system is

$$-\frac{\partial \boldsymbol{\lambda}_k}{\partial t} = \left(\mathbf{A}\left[\mathbf{u}^b\right]\right)'\boldsymbol{\lambda}_k + \mathbf{q}_k(t), \tag{A1}$$

$$\boldsymbol{\lambda}_k(T) = 0 \tag{A2}$$

and the TL system is

$$\frac{\partial \mathbf{r}_k}{\partial t} = \mathbf{A}[\mathbf{u}^b]\mathbf{r}_k, \tag{A3}$$

$$\mathbf{r}_k(0) = \mathbf{C}_0 \boldsymbol{\lambda}_k(0). \tag{A4}$$

If the number of observations K is small enough, a representer for each observation can be computed. Then, the $K \times K$ symmetric and nonnegative representer matrix $\mathbf{R}$ is formed, with elements

$$R_{km} = L_k \mathbf{r}_m \tag{A5}$$

and the optimal set of the representer coefficients $\mathbf{b} = \{b_k\}$ is determined solving the following discrete system of equations:

$$(\mathbf{R} + \mathbf{C}_d)\mathbf{b} = \mathbf{d} - L\mathbf{u}^b. \tag{A6}$$

Then, the optimal correction to the initial conditions is $\sum_{k=1}^{K} b_k \mathbf{r}_k(0)$.

[49] In this study, we implement an indirect representer method [*Egbert et al.*, 1994] that does not require explicit computation and storage of each representer and thus can be utilized with large data sets. The linear system (A6) is solved iteratively using the conjugate gradient method [e.g., *Golub and van Loan*, 1989] that does not require explicit knowledge of $\mathbf{P} = \mathbf{R} + \mathbf{C}_d$, but only an algorithm that computes the product $\mathbf{P}\beta$, where β is any vector of size K. We have used diagonal $\mathbf{C}_d$, such that computation of $\mathbf{C}_d\beta$ is trivial. The product $\mathbf{R}\beta$ is obtained using one ADJ and one TL model run, as follows. The ADJ model (4) is run with β_k replacing $\mathbf{b}_k$. Then the TL model (A3) is run with initial conditions $\mathbf{C}_0\boldsymbol{\lambda}(0)$. Finally, the result of the TL computation, say $\mathbf{r}(t)$, is sampled using the data operator: $\mathbf{R}\beta = L\mathbf{r}$. In our cases, the conjugate gradient algorithm is started in each time window with the initial guess $\mathbf{b} = 0$ and terminated when

$$\omega = \frac{\|\mathbf{d} - L\mathbf{u}^b - \mathbf{Pb}\|^2}{\|\mathbf{d} - L\mathbf{u}^b\|^2} < 10^{-3}, \tag{A7}$$

where $\|\mathbf{a}\|^2 = \mathbf{a}'\mathbf{a}$. In cases involving assimilation of SSH alone, K is between 100 and 200 in every assimilation window, and the minimization algorithm converges rapidly, in 5–10 iterations. In cases involving combined SSH and SST assimilation, with $K \approx 10,000$, the preconditioned conjugate gradient method is utilized [see *Golub and van Loan*, 1989]. The preconditioner matrix, which approximates $\mathbf{P}$ and is easy to invert, has been built using a subset of 90–140 representers computed explicitly [*Egbert and Bennett*, 1996; *Egbert*, 1997; *Bennett*, 2002, section 3.1.5]. With this preconditioner, the minimization algorithm converged in 5–10 iterations.

Appendix B: The Balanced Operator

[50] Here we explain details of the balance operator implementation (6) that allows estimating perturbations $\delta\zeta$, δu, δv, and δS given perturbations in the the depth-integrated transport stream function $\delta\Psi$ and temperature δT, using simplified, linear diagnostic relations. We have generally followed the idea of *Weaver et al.* [2005].

[51] The salinity and temperature perturbations are assumed to satisfy the simple *T-S* relation

$$\delta S = \alpha \delta T, \tag{B1}$$

with $\alpha = -0.16$ psu C^{-1}, based on the analysis of the free run model profiles. The density perturbation $\delta\rho$ is then computed using the linearized equation of state

$$\delta\rho = \rho_\circ(-\alpha_T \delta T + \alpha_S \delta S), \tag{B2}$$

where $\rho_\circ = 1025$ kg m^{-3}, $\alpha_T = 1.7 \times 10^{-4}$ C^{-1}, and $\alpha_S = 7.5 \times 10^{-4}$ psu^{-1}. To find $\delta\zeta$, *Weaver et al.* [2005] integrate $\delta\rho$ from the reference depth, where $(\delta u, \delta v) = 0$. They note that this method would not work over the shelf, where no reference depth can be defined. Following their guidance, the second-order elliptic equation for $\delta\zeta$ is solved instead [*Fukumori et al.*, 1998]. In our case, the geostrophic relation is

$$f \mathbf{k} \times (\delta u, \delta v) = -g\nabla\delta\zeta - \frac{g}{\rho_\circ} \int_z^0 \nabla\delta\rho \, dz', \tag{B3}$$

where ∇ denotes the horizontal gradient operator and $\mathbf{k}$ the vertical unit vector. We will assume that the vertically integrated transport correction has zero divergence, use the stream function definition

$$\mathbf{k} \times \nabla\delta\Psi = -\int_{-H}^0 (\delta u, \delta v) dz \tag{B4}$$

and integrate (B3) in the vertical to obtain

$$-f\nabla\delta\Psi = -gH\nabla\delta\zeta - \frac{g}{\rho_\circ} \int_{-H}^0 dz \int_z^0 \nabla\delta\rho \, dz'. \tag{B5}$$

We take divergence of (B5) to obtain the equation for $\delta\zeta$

$$g\nabla \cdot (H\nabla\delta\zeta) = \delta F_\Psi - \delta F_\rho, \tag{B6}$$

where

$$\delta F_\Psi = \nabla \cdot (f\nabla\delta\Psi), \tag{B7}$$

$$\delta F_\rho = \frac{g}{\rho_\circ} \nabla \cdot \left(\int_{-H}^0 dz \int_z^0 \nabla\delta\rho \, dz' \right). \tag{B8}$$

Equation (B6) is solved by direct factorization [*Golub and van Loan*, 1989], using $\delta\zeta = 0$ around the boundary. Along open ocean segments, this boundary condition is chosen since SSH is not varied at the boundary at any time. If no geostrophic flow is assumed across the coast, $\partial\zeta/\partial l = 0$, where l is the coordinate along the coast. Then, for consistency with the open boundaries, $\zeta = 0$ along the coast as well. Fields of δu and δv can then be obtained from (B3).

[52] In AVRORA, the balance operator is implemented as a FORTRAN code that yields fields on the left hand side of (6) given arbitrary input fields of δT and $\delta\Psi$. The covariance implementation requires computation of matrix-vector products using not only $\mathbf{B}$, but also its adjoint $\mathbf{B}'$ (7). The adjoint FORTRAN code, multiplying $\mathbf{B}'\boldsymbol{\lambda}(0)$, is developed by applying rules of adjoint code transformation [*Giering*

and Kaminski, 1998] to the balance operator code, exactly as ADJ AVRORA has been built.

References

Bennett, A. F. (2002), *Inverse Modeling of the Ocean and Atmosphere*, 234 pp., Cambridge Univ. Press, Cambridge, U. K.

Bennett, A. F., B. S. Chua, B. L. Pflaum, M. Erwig, Z. Fu, R. D. Loft, and J. C. Muccino (2008), The inverse ocean modeling system. Part I: Implementation, *J. Atmos. Oceanic Technol.*, 25, 1608–1622.

Brink, K. H. (1991), Coastal-trapped waves and wind-driven currents over the continental shelf, *Ann. Rev. Fluid Mech.*, 23, 389–412.

Brink, K. H., and T. J. Cowles (1991), The coastal transition zone program, *J. Geophys. Res.*, 96, 14,637–14,647.

Broquet, G., C. A. Edwards, A. M. Moore, B. S. Powell, M. Veneziani, and J. D. Doyle (2009), Application of 4D-variational data assimilation to the California Current System, *Dyn. Atmos. Oceans*, 48, 69–92, doi:10.1016/j.dynatmoce.2009.03.001.

Chua, B., and A. F. Bennett (2001), An inverse ocean modeling system, *Ocean Modell.*, 3, 137–165.

Di Lorenzo, E., A. M. Moore, H. G. Arango, B. D. Cornuelle, A. J. Miller, B. Powell, B. S. Chua, and A. F. Bennett (2007), Weak and strong constraint data assimilation in the inverse Regional Ocean Modeling System (ROMS): Development and application for a baroclinic coastal upwelling system, *Ocean Modell.*, 16, 160–187, doi:10.1016/j.ocemod.2006.08.002.

Egbert, G. D. (1997), Tidal data inversion: Interpolation and inference, *Prog. Oceanogr.*, 40, 53–80.

Egbert, G. D., and A. F. Bennett (1996), Data assimilation methods for ocean tides, in *Modern Approaches to Data Assimilation in Ocean Modeling*, edited by P. Malanotte-Rizzoli, pp. 147–179, Elsevier, Amsterdam.

Egbert, G. D., A. F. Bennett, and M. G. G. Foreman (1994), TOPEX/POSEIDON tides estimated using a global inverse model, *J. Geophys. Res.*, 99, 24,821–24,852, doi:10.1029/94JC01894.

Fairall, C. W., E. F. Bradley, D. P. Rogers, J. B. Edson, and G. S. Young (1996), Bulk parameterization of air-sea fluxes for TOGA COARE, *J. Geophys. Res.*, 101, 3747–3767.

Fukumori, I., R. Raghunath, and L.-L. Fu (1998), Nature of global large-scale sea level variability in relation to atmospheric forcing: A modeling study, *J. Geophys. Res.*, 103, 5493–5512.

Giering, R., and T. Kaminski (1998), Recipes for adjoint code construction, *Assoc. Comput. Mach. Trans. Math. Software*, 24, 437–474.

Golub, G. H., and C. F. van Loan (1989) *Matrix Computations*, 2nd ed., 642 pp., John Hopkins Univ. Press, Baltimore, Md.

Kim, S., R. M. Samelson, and C. Snyder (2009), Ensemble-based estimates of the predictability of wind-driven coastal ocean flow over topography, *Mon. Weather Rev.*, 137, 2515–2537, doi:10.1175/2009MWR2631.1.

Koch, A. O., A. L. Kurapov, and J. S. Allen (2010), Near-surface dynamics of a separated jet in the coastal tranzition zone off Oregon, *J. Geophys. Res.*, 115, C08020, doi:10.1029/2009JC005704.

Kosro, P. M., W. T. Peterson, B. M. Hickey, R. K. Shearman, and S. D. Pierce (2006), Physical versus biological spring transition: 2005, *Geophys. Res. Lett.*, 33, L22S03, doi:10.1029/2006GL027072.

Kurapov, A. L., J. S. Allen, R. N. Miller, and G. D. Egbert (1999), Generalized inverse for baroclinic coastal flows, paper presented at 3rd Conference on Coastal Atmospheric and Oceanic Prediction and Processes, Am. Meteorol. Soc., New Orleans, La., 3–5 Nov.

Kurapov, A. L., G. D. Egbert, R. N. Miller, and J. S. Allen (2002), Data assimilation in a baroclinic coastal ocean model: Ensemble statistics and comparison of methods, *Mon. Weather Rev.*, 130, 1009–1025.

Kurapov, A. L., J. S. Allen, G. D. Egbert, R. N. Miller, P. M. Kosro, M. Levine, and T. Boyd (2005a), Distant effect of assimilation of moored currents into a model of coastal wind-driven circulation off Oregon, *J. Geophys. Res.*, 110, C02022, doi:10.1029/2003JC002195.

Kurapov, A. L., J. S. Allen, G. D. Egbert, R. N. Miller, P. M. Kosro, M. Levine, T. Boyd, and J. A. Barth (2005b), Assimilation of moored velocity data in a model of coastal wind-driven circulation off Oregon: Multivariate capabilities, *J. Geophys. Res.*, 110, C10S08, doi:10.1029/2004JC002493.

Kurapov, A. L., J. S. Allen, G. D. Egbert, and R. N. Miller (2005c), Modeling bottom mixed layer variability on the mid-Oregon shelf during summer upwelling, *J. Phys. Oceanogr.*, 35, 1629–1649.

Kurapov, A. L., G. D. Egbert, J. S. Allen, and R. N. Miller (2009), Representer-based analyses in the coastal upwelling system, *Dyn. Atmos. Oceans*, 48, 198–218, doi:10.1016/j.dynatmoce.2008.09.002.

Li, Z., Y. Chao, J. C. McWilliams, and K. Ide (2008), A three-dimensional variational data assimilation scheme for the Regional Ocean Modeling System: Implementation and basic experiments, *J. Geophys. Res.*, 113, C05002, doi:10.1029/2006JC004042.

Mellor, G. L., and T. Yamada (1982), Development of a turbulent closure model for geophysical fluid problems, *Rev. Geophys.*, 20, 851–875.

Ngodock, H. E., S. R. Smith, and G. A. Jacobs (2007), Cycling the representer algorithm for variational data assimilation with a nonlinear reduced gravity ocean model, *Ocean Modell.*, 19, 101–111, doi:10.1016/j.ocemod.2007.06.004.

Oke, P. R., J. S. Allen, R. N. Miller, G. D. Egbert, and P. M. Kosro (2002), Assimilation of surface velocity data into a primitive equation coastal ocean model, *J. Geophys. Res.*, 107(C9), 3122, doi:10.1029/2000JC000511.

Oliger, J., and A. Sundström (1978), Theoretical and practical aspects of some initial boundary value problems in fluid dynamics, *SIAM J. Appl. Math.*, 35, 419–446.

Pierce, S. D., J. A. Barth, R. E. Thomas, and G. W. Fleischer (2006), Anomalously warm July 2005 in the northern California Current: Historical context and the significance of cumulative wind stress, *Geophys. Res. Lett.*, 33, L22S04, doi:10.1029/2006GL027149.

Powell, B. S., A. M. Moore, H. G. Arango, E. Di Lorenzo, R. F. Milliff, and R. R. Leben (2009), Near real-time assimilation and prediction in the Intra-Americas Sea with the Regional Ocean Modeling System (ROMS), *Dyn. Atmos. Oceans*, 48, 46–68. doi:10.1016/j.dynatmoce.2009.04.001

Schwing, F. B., N. A. Bond, S. J. Bograd, T. Mitchell, M. A. Alexander, and N. Mantua (2006), Delayed coastal upwelling along the U.S. West Coast in 2005: A historical perspective, *Geophys. Res. Lett.*, 33, L22S01, doi:10.1029/2006GL026911.

Shulman, I. G., J. C. Kindle, S. DeRada, S. C. Anderson, and B. Penta (2004), Development of a hierarchy of nested models to study the California Current System, in *Estuarine and Coastal Modeling: Proceedings of the Eighth International Conference, November 3–5, 2003, Monterey, California*, edited by M. L. Spaulding, pp. 74–88, doi:10.1061/40734(145)6, Am Soc. of Civ. Eng., Reston, Va.

Springer, S. R., R. M. Samelson, J. S. Allen, G. D. Egbert, A. L. Kurapov, R. N. Miller, and J. C. Kindle (2009), A nested grid model of the Oregon coastal transition zone: Simulations and comparisons with observations during the 2001 upwelling season, *J. Geophys. Res.*, 114, C02010, doi:10.1029/2008JC004863.

Weaver, A. T., C. Deltel, E. Machu, S. Ricci, and N. Daget (2005), A multivariate balance operator for variational ocean data assimilation, *Q. J. R. Meteorol. Soc.*, 131, 3605–3625.

Wijesekera, H. W., J. S. Allen, and P. A. Newberger (2003), Modeling study of turbulent mixing over the continental shelf: Comparison of turbulent closure schemes, *J. Geophys. Res.*, 108(C3), 3103, doi:10.1029/2001JC001234.

Xu, L., and R. Daley (2000), Towards a true 4-dimensional data assimilation algorithm: Application of a cycling representer algorithm to a simple transport problem, *Tellus Ser. A*, 52, 109–128.

J. S. Allen, G. D. Egbert, A. L. Kurapov, and P. T. Strub, College of Oceanic and Atmospheric Sciences, Oregon State University, 104 COAS Administration Bldg., Corvallis, OR 97331-5503, USA. (kurapov@coas.oregonstate.edu)

D. Foley, Environmental Research Division, NOAA Southwest Fisheries Science Center, 1352 Lighthouse Ave., Pacific Grove, CA 93950-2097, USA.